

THESIS FOR THE DEGREE OF LICENTIATE OF ENGINEERING

Atomic-scale modelling of interfaces in cemented  
carbides: wetting and strength

MARTIN A. GREN

*Department of Physics*

CHALMERS UNIVERSITY OF TECHNOLOGY

Göteborg, Sweden 2017

Atomic-scale modelling of interfaces in cemented carbides: wetting and strength  
MARTIN A. GREN  
Göteborg, 2017

© Martin A. Gren, 2017

Department of Physics  
Chalmers University of Technology  
SE-412 96 Göteborg, Sweden  
Telephone +46 31 772 10 00

Cover: Binder phase spreading on a WC surface (top left), binder phase droplet on a WC surface with the contact angle  $\theta$  (top right), and WC/WC grain boundary before and after infiltration by the binder phase (bottom).

Chalmers reproservice  
Göteborg, Sweden 2017

# Atomic-scale modelling of interfaces in cemented carbides: wetting and strength

MARTIN A. GREN

*Department of Physics*

Chalmers University of Technology

---

## **Abstract**

Cemented carbides are composite materials of great technological and industrial importance. They have a unique combination of hardness and toughness and are therefore used widely as tool materials in applications where both high hardness and toughness are demanded. These applications include among others: mining, turning, cutting and milling. Cemented carbides are powder metallurgical products where powders are mixed, pressed, and sintered into a dense material. These materials consists of a hard carbide phase embedded in a more ductile metal binder phase.

The interfaces in cemented carbides highly influence the behavior during sintering and consequently the microstructure of the final material. Further, the unique mechanical properties of cemented carbides are to a large degree dependent on its microstructure and the stability and strength of its interfaces.

This thesis is a computational study of interfaces in WC–Co, WC–Fe, and WC–Ni cemented carbides. Density functional theory is used to calculate interface energies and the local chemistry of interfaces is varied by altering the termination of WC planes and by substitution of W and C atoms for binder phase atoms.

In paper I we investigate wetting of WC surfaces and WC/WC grain boundaries by the binder phase, and the results indicate that the wettability of Ni on WC surfaces is potentially better compared to that of Co, which in turn is better than that of Fe. Additionally, the wetting of WC surfaces is better in W-rich alloys compared to C-rich alloys regardless of binder, which is in agreement with experiments on wetting in WC–Co cemented carbides.

In paper II the segregation to WC/WC grain boundaries and its effect on the interface strength is investigated. We show that the segregation of binder phase atoms to WC/WC grain boundaries is in 0.5 monolayer proportion in essentially all studied grain boundaries in the three different cemented carbides. The segregation generally strengthens the grain boundaries regarding its resistance against fracture and infiltration by binder phase.

**Keywords:** cemented carbides, hardmetals, WC-Co, density functional theory, interfaces, grain boundaries, surfaces, phase boundaries, wetting, adhesion



## LIST OF PUBLICATIONS

This thesis consists of an introductory text and the following papers:

**I Wetting of surfaces and grain boundaries in cemented carbides**

M. A. Gren and G. Wahnström

In manuscript

**II Grain boundary segregation and strength in cemented carbides**

M. A. Gren, M. V. G. Petisme, and G. Wahnström

In manuscript

Scientific papers not included in this thesis:

**III Molecular dynamics simulation of WC/WC grain boundary sliding resistance in WC–Co cemented carbides at high temperature.**

M. V. G. Petisme, M. A. Gren, and G. Wahnström

International Journal of Refractory Metals and Hard Materials 49 (2015).

Specification of my contribution to the appended papers:

- I Did all the calculations and wrote the paper.
- II Did most of the calculations and co-wrote the paper.



# Contents

<b>1</b>	<b>Introduction</b>	<b>1</b>
<b>2</b>	<b>Cemented carbides</b>	<b>5</b>
2.1	Manufacturing . . . . .	7
2.1.1	Powders . . . . .	7
2.1.2	Milling, drying, pressing . . . . .	8
2.1.3	Sintering . . . . .	9
2.1.4	Finishing and coating . . . . .	11
2.1.5	Densification process . . . . .	11
2.1.6	Controlling the phase constitution . . . . .	14
<b>3</b>	<b>Microstructure of cemented carbides</b>	<b>17</b>
3.1	Hard phase - Tungsten carbide . . . . .	18
3.2	Binder phase . . . . .	20
3.2.1	Cobalt . . . . .	20
3.2.2	Nickel . . . . .	22
3.2.3	Iron . . . . .	22
3.3	Interfaces in cemented carbides . . . . .	23
3.3.1	WC/WC grain boundaries . . . . .	24
3.3.2	WC/Co phase boundaries . . . . .	27
<b>4</b>	<b>Model geometries of interfaces in cemented carbides</b>	<b>31</b>
4.1	WC/WC grain boundaries . . . . .	31
4.1.1	$\Sigma = 2$ model grain boundaries . . . . .	32
4.1.2	$\Sigma = 4$ model grain boundaries . . . . .	33
4.2	WC/Binder phase boundaries . . . . .	35
4.3	Surfaces . . . . .	36
4.4	Adsorption and segregation . . . . .	36
<b>5</b>	<b>Thermodynamics of interfaces</b>	<b>39</b>
5.1	Interface free energy . . . . .	39

5.1.1	Implementation in DFT . . . . .	40
5.2	Interface stress . . . . .	42
5.3	Wetting of surfaces . . . . .	43
5.3.1	Wetting of grain boundaries . . . . .	46
5.3.2	Effect from adsorption and segregation . . . . .	49
5.4	WC/WC grain boundary strength . . . . .	50
5.4.1	Work of adhesion . . . . .	50
5.4.2	Work of separation . . . . .	52
5.4.3	Work of infiltration by the binder phase . . . . .	52
<b>6</b>	<b>Conclusions and outlook</b>	<b>55</b>
<b>A</b>	<b>Computational method</b>	<b>57</b>
	<b>Acknowledgments</b>	<b>59</b>
	<b>Bibliography</b>	<b>61</b>
	<b>Papers I-II</b>	<b>71</b>

# Introduction

Cemented carbides, or hardmetals, are composite materials with a unique combination of hardness and toughness [1]. In materials the *hardness* (the ability to resist plastic deformation by a certain load) and the *toughness* (the ability to absorb energy by deforming plastically without failure) are two competing properties, i.e. a material usually is hard and brittle or tough and soft. In Fig. 1.1, the hardness vs. toughness for variety of hard materials is shown. We see that the extremely hard diamond is also highly brittle and the high-speed steels (HSS) are tougher but lack in hardness. However, cemented carbides manages to be simultaneously very hard and tough, which makes them a unique class of materials.

Cemented carbides consists of two main components: a hard component, tungsten carbide (WC), and a more ductile binder component, which in a vast majority of cases is cobalt (Co). These composite materials are manufactured by means of powder metallurgy, where powders of tungsten carbide and binder metal are mixed, pressed, and sintered into a dense material [3]. In the microstructure of cemented carbides both the WC and binder grains are interconnected and build up two continuous inter-penetrating skeletons. In this way the hardness and toughness from the WC phase and the binder phase, respectively, are combined without too much loss, leading to both high hardness and toughness. Further, the hardness and toughness of the cemented carbide can be adjusted by varying the WC grain size and the binder content.

These material properties makes cemented carbides an excellent choice of material in application where high wear-resistance and toughness are crucial [4]. Consequently, cemented carbide is the most widely used material for various metal machining operations such as turning, milling, drilling, threading, grooving, etc. A picture of a turning operation using the Sandvik Coromant CoroTurn® Prime is seen in Fig. 1.2. As the cemented carbides are of such technological importance,

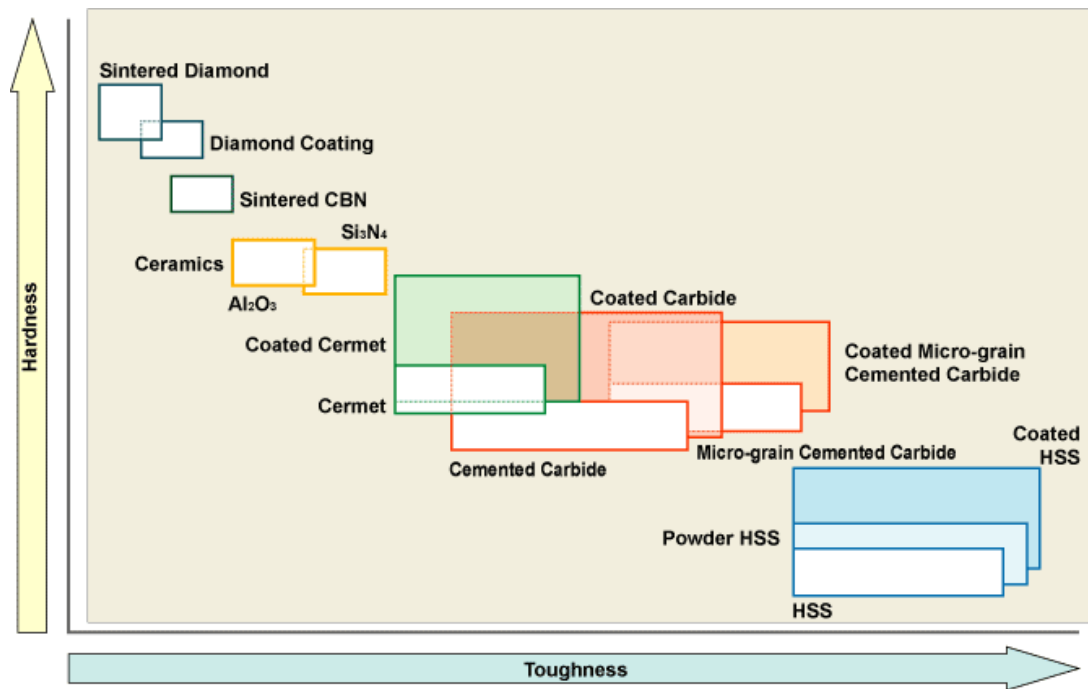


Figure 1.1: Sketch of the hardness vs. toughness for different types of hard materials [2].

there is a great competition within the industry to improve and develop new grades. In the recent times cobalt has also been found to be toxic and carcinogenic, especially in the form of (WC–Co) hardmetal dust [6]. There is, therefore, also a large interest in replacing Co as the primary binder phase.

As the computational power of computers and the efficiency of the theoretical tools have increased rapidly in the last decades, atomistic simulation methods are becoming increasingly important in materials science. Density functional theory (DFT) now allows us to calculate material properties direct from first principles. It has a great predictive power and can, in cases that are difficult to approach experimentally, provide crucial insights on the atomic and electronic level. In cemented carbides the thermodynamics of interfaces are important both for the manufacturing and the mechanical properties of the material. Additionally, interfacial energies are hard to measure experimentally and in most cases one has to rely on estimations. To study interfacial energetics in cemented carbides, DFT calculations, therefore, serves as an important tool.

In this thesis the density functional theory is used to study interfaces in WC–Fe, WC–Co, and WC–Ni cemented carbides. Paper I is an investigation of wetting of WC surfaces and WC/WC grain boundaries in cemented carbides, while paper II investigates the segregation of binder phase atoms to WC/WC grain boundaries



Figure 1.2: A turning operation using the Sandvik Coromant CoroTurn® Prime [5].

and its effect on the interface strength. In both papers, the local chemistry of the interfaces is varied by altering the termination of WC planes and substituting W or C atoms for binder phase atoms.



## Cemented carbides

Cemented carbides are composite materials with one hard component, the carbide, and one more ductile binder component which acts as cement between the carbide grains, and hence the name cemented carbides [3]. The hard component is usually tungsten carbide (WC) and the binder is usually cobalt (Co). These composite materials are manufactured by means of powder metallurgy, where powders of tungsten carbide and binder metal are mixed and milled, then pressed and finally sintered. The sintering is done at temperatures in the interval 1350 to 1500 °C where the binder phase is molten, which accelerates the densification and this results in a material with almost 100% of theoretical density. The resulting material consists of a continuous skeleton of hard phase WC grains inside a matrix of ductile binder phase, where the former serves to give the material significant hardness and wear resistance, while the later gives increased toughness [1]. This combination of both high hardness and toughness makes cemented carbides unique among hard materials, see Fig. 1.1. The hardness and toughness of the cemented carbide can also be adjusted by varying the WC grain size and the binder content.

When manufacturing cemented carbides it is important to control the phase constitution to avoid deteriorating phases [7]. The desired phases in the microstructure of cemented carbides are hexagonal WC and fcc binder [8]. The phase constitution is to large degree controlled by the amount carbon (carbon activity) in the material and small changes in the amount of carbon may have large effects on the phase constitution. If the amount of carbon is too high, graphite will form in material, and if the amount of carbon is too low, complex carbides called eta phases will form. Both of these are considered to be deteriorating for the material properties [7]. There is thus a window of carbon contents within which no graphite, nor eta phase, is formed in the material. This window is bound by the graphite and eta limits, which mark the carbon contents where the respective phases are formed.

In this theses we refer to a material with a high carbon content as C-rich and a material with a low carbon content as W-rich.

Originally, in the 1920s, cemented carbides were developed in order to replace diamond in drawing dies for tungsten filament production [3]. However, it was soon realized that the main application for this material was metal cutting and rock drilling. The new cemented carbides radically outperformed the usual alloyed steels and stellites, which reduced the cost drastically, leading to a big increase in productivity. Today, cemented carbide is the most widely used material for various metal machining operations such as cutting, turning, milling, drilling, threading, grooving, etc. [4].

Ever since Karl Schröter proposed to bind tungsten carbide with cobalt in 1923, cobalt has been the traditional choice as binder metal [9]. A combination of its excellent mechanical properties and wetting of WC makes it a very good binder metal. Furthermore, it is less challenging to get a material free from graphite and  $\eta$  phase compared to other binders such as nickel and iron [8]. Although the occurrence of cobalt in the earth's crust is only slightly less than zinc or lead, the main ore deposits are located in areas less accessible to the industrial world, mainly in Central Africa [9, 10]. The price and supply of cobalt is therefore subject to large fluctuations. In the recent times cobalt has also been found to be toxic and carcinogenic, especially in the form of (WC-Co) hardmetal dust [6]. Consequently, there is a large drive for replacing cobalt completely or partially as binder. Initially, though, research was dedicated to replacing cobalt in order to avoid the early patent restrictions [10].

Historically nickel has received the most attention as an alternative binder to cobalt due to its similar properties [8]. A complete substitution of cobalt for nickel results in material with inferior hardness and strength due to the more ductile binder phase [9]. The higher stacking fault energy of Ni also makes the work hardening moderate compared to Co [6]. However, the fracture toughness and the wear resistance are improved and the corrosion and oxidation resistance is superior to cobalt bound cemented carbides [9, 8, 6]. Consequently, nickel is almost exclusively used as binder material in die and wear parts. It is important to note that the toxicity of Ni is at the same level as Co which could limit further development of pure Ni bound cemented carbides [6].

Cemented carbides with certain Fe-Ni-Co binder compositions have been shown to be of interest for the hard metal industry, especially in applications where improved fatigue strength and toughness are required [6]. However, it is very demanding to produce defect free iron bonded materials due to the narrow carbon window. Further, Fe bound alloys have a tendency to form martensite and react with Fe-based workpieces during machining operations. The usage of iron based binders in cemented carbides is, however, predicted to grow due to its superiority in certain applications and its more environmentally friendly nature compared to

Ni and Co [4]. A further driving force is the superior availability of iron compared to nickel and cobalt.

Other examples of alternative binder compositions are nickel aluminides ( $\text{Ni}_3\text{Al}$  and  $\text{NiAl}$ ) and iron aluminides ( $\text{Fe}_3\text{Al}$  and  $\text{FeAl}$ ). These binders are suitable in high-temperature applications and extremely corrosive environments [11, 12, 13, 14].

As cobalt is and has been the most common binder in cemented carbides for a long time, most of the research on cemented carbides has been directed towards improving and understanding WC–Co based cemented carbides. There is thus much more knowledge of the properties and production of cemented carbides with cobalt as binder compared to other binder compositions. It is the authors' opinion that this acts as a lock-in mechanism that prevents the industry from moving away from cobalt as a binder, even though alternatives with comparable or sometimes superior properties exist. Research on alternative binders is therefore of great importance.

Similar to cobalt, tungsten is also found in areas less available to most of the industrial world, with the main deposits being located in China and Eastern Europe [10]. Consequently, there has also been development towards replacing the WC hard phase by TiC, which culminated in TiCN cermets.

## 2.1 Manufacturing

Cemented carbides are produced by means of powder metallurgy, where metal and carbide powders are mixed and heated to form a dense material. There are many steps in the process from raw material to finished product and all of these steps affect, to a varying degree, the microstructure of the final material [15, 16].

### 2.1.1 Powders

WC powder is most commonly produced by carburization of tungsten metal powder prepared by hydrogen reduction of  $\text{WO}_3$  [17]. It is also possible to carburize and reduce  $\text{WO}_3$  simultaneously. The primary sources of the tungsten are the minerals Scheelite ( $\text{CaWO}_4$ ) and Wolframite ( $(\text{Fe},\text{Mn})\text{WO}_4$ ). The typical grain size of conventionally produced WC powder ranges between 0.15 to 12  $\mu\text{m}$  [18]. A scanning electron microscope (SEM) micrograph of a WC powder with grain sizes in the sub-micron range is seen in Fig. 2.1.

Cobalt, the most common binder, is mainly produced as the by-products of more common copper and nickel metals or from re-cycling of cemented carbide scrap due to a scarcity of cobalt ores [20]. Pure cobalt compounds are produced by hydrometallurgical processing of cobalt from the ores and scrap. These compounds are then reduced to form cobalt powders.

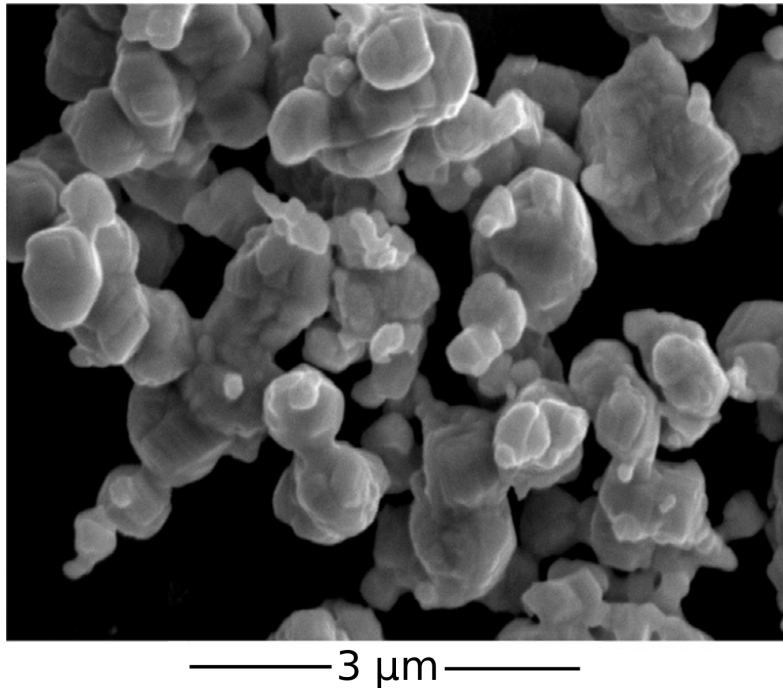


Figure 2.1: WC powder with grain sizes in the submicron range [19].

Most powders of carbide and binder phases are available as commercial products. Consequently, to choose the powders that will be used is the first stage in the manufacturing of cemented carbides [19]. Selection of the correct powder is critical in order to achieve the required quality in the final sintered product, meet the cost targets and accommodate subsequent process requirements. The quality of the powders is determined by the composition, particle size, morphology, surface chemistry, etc.

### 2.1.2 Milling, drying, pressing

As the first step in consolidating the cemented carbide, the powders are mixed together and thereafter milled [19, 7, 17]. The purpose of the milling is to get a more uniform mixing of the powders, reduce particle size to a desired value, and to reduce agglomeration of WC particles. It is critical to get the mixing uniform since it determines reliability and repeatability of properties and performance of the final products. For example, an insufficient mixing of binder and carbide may lead to defects such as porosity and binder metal pools. The most common milling methods are rolling ball milling and attritor milling, and each of these methods has its own particular milling characteristic. For example, rolling ball milling generally gives a more narrow particle size distribution than attritor milling, but the milling

time is considerably longer. Rolling ball milling is effective in reducing the particle sizes down to roughly  $2\ \mu\text{m}$ , while attritor milling can produce finer particle sizes. The energy involved in milling is high, and it is therefore necessary to carry out the milling in a protective liquid to minimize temperature rise and prevent oxidation [17]. Often, an organic liquid such as acetone or alcohol is used. In order to improve the strength of the material after the forthcoming pressing, organic binders such as paraffin wax or polyethylene glycol is also added in the milling stage [19]. Additionally, to facilitate the mixing and particle deagglomeration, and to reduce particle size by crushing and attrition, a milling media is also added to the mill. This milling media often consists of bodies of WC-Co [21].

When the slurry of carbide and binder grains obtained after milling is dried the resulting powder is very fine. The powder therefore have a low flowability and a low apparent density which is not desirable for pressing [17]. To avoid this, a process called *granulation* is adopted, where the objective is to create loose agglomerates of the fine powder. The old conventional method of granulation is to first boil off the solvent in a vacuum, then press the powder into billets. These billets are thereafter disintegrated and finally particles of the desired size are sieved in filterers. In the modern and more direct method, spray drying, the slurry is dried and granulated by spraying it into a stream of preheated inert gas. This method of granulation generates granules of uniform size and nearly spherical shape which is favourable for the pressing stage.

After the granulation the powder is ready to be pressed into a compact called a *green body*. Common methods for shaping the green body are uniaxial die pressing, cold isostatic pressing, extrusion and powder injection molding [7]. Die pressing is, however, the most widely used and economical method of shaping in the cemented carbide industry. Usually, the pressures used in pressing are in the range of 30-200 MPa. The green body can be shaped close to the desired final shape as shape is approximately maintained during sintering. However, one has to compensate for the substantial linear shrinkage of roughly 20% [18, 21]. A picture of green body and sintered material which demonstrates this shrinkage can be seen in Fig. 2.2.

### 2.1.3 Sintering

The purpose of the sintering stage is to strengthen the material through densification, thus eliminating pores, and by creating strong intergrain cohesion. To accomplish this, the green body is heated in a furnace where the temperature and atmosphere is well-controlled. The temperature progression of a typical sintering cycle of a WC-Co cemented carbide can be seen in Fig. 2.3. First, the temperature is slowly raised to approximately  $300\ ^\circ\text{C}$ , during which, the organic binder is removed ("de-waxing") [21]. A hydrogen atmosphere is often used in this stage. Thereafter, the furnace is evacuated and the atmosphere is kept as vacuum if no

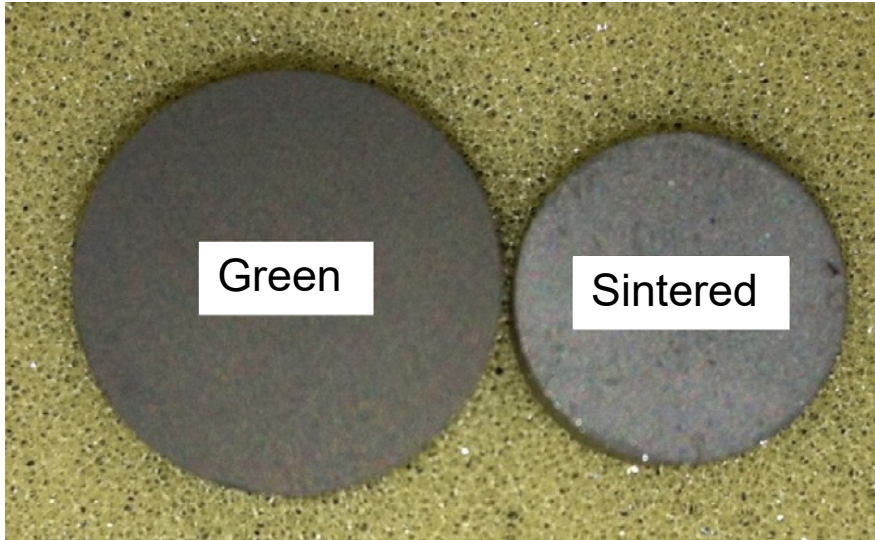


Figure 2.2: Example of shrinkage as a result of sintering [19]. Green body (left) and the corresponding sintered material (right).

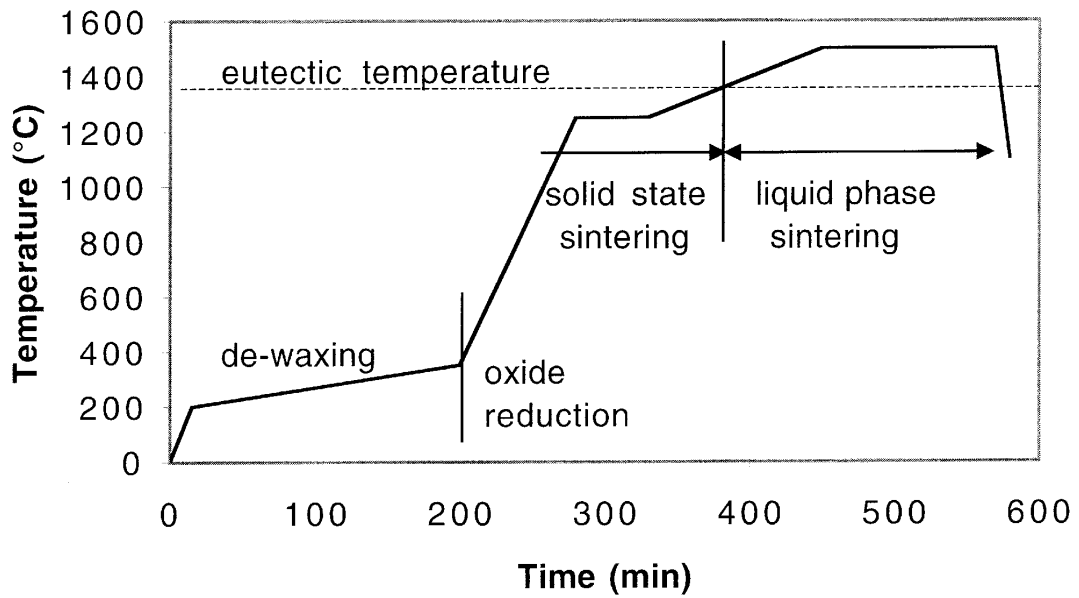


Figure 2.3: Typical sintering cycle for WC-Co [21].

other atmosphere is needed. This is followed by a raise in temperature to approximately 1200 °C. Since the pores are still opened at this stage, oxygen reduction can take place. The temperature is kept at 1200 °C for some time and solid-state sintering occurs, which actually is responsible for more than half of the total densification during the entire sintering [17]. At this point the W and C also start dissolving in the binder [21]. Now, the temperature is raised to and kept at about 1400-1500 °C, which is above the eutectic temperature. Consequently, the binder melts which onsets the liquid-phase sintering. W and C dissolves further in the liquid binder and the remaining porosity is almost completely eliminated. During the liquid-phase sintering, a lot of the WC grain growth takes place through solution-precipitation. To restrict the grain growth during sintering, small amounts of certain carbides such as  $\text{Cr}_3\text{C}_2$ , TiC, and VC may be added in the milling stage. Finally, the material is cooled down. This vacuum sintering method works well for materials where wetting is excellent, however, if wetting is poorer, hot isostatic pressure (HIP) sintering may be used to achieve full densification.

#### 2.1.4 Finishing and coating

Due to the shrinkage during sintering many materials often need finishing after sintering. Since the cemented carbides are very hard, diamond abrasives are often used for the machining. A majority of cutting tools made from WC-Co are coated by a thin film of ceramic material, using either physical vapor deposition (PVD) or chemical vapor deposition (CVD) [7]. The coated materials have a higher wear resistance and potentially better chemical stability which prolongs the lifetime of tools considerably.

#### 2.1.5 Densification process

The driving force for sintering, both in solid and liquid state, is the reduction of interface energy in the system [22]. The reduction of interface energy can be accomplished by either reducing the total interface area or equilibration of the interfaces to more favourable configurations. This induces a mass transport which leads to densification and grain growth. The densification process during sintering is depicted in Fig. 2.4.

Initially the mix of powders contain lots of porosities, which are reduced during solid-state sintering when the facets of WC grains are optimized and phase boundaries between WC and binder are formed as the binder wets the carbide [22]. It has been suggested that Co spreading on WC is preceded by a fast moving precursor film of sub-monolayer thickness, on top of which the Co front may flow easily [23].

Upon the subsequent melting of the binder phase WC grains become more mobile and capillary forces pull the solid grains together which further densifies the mate-

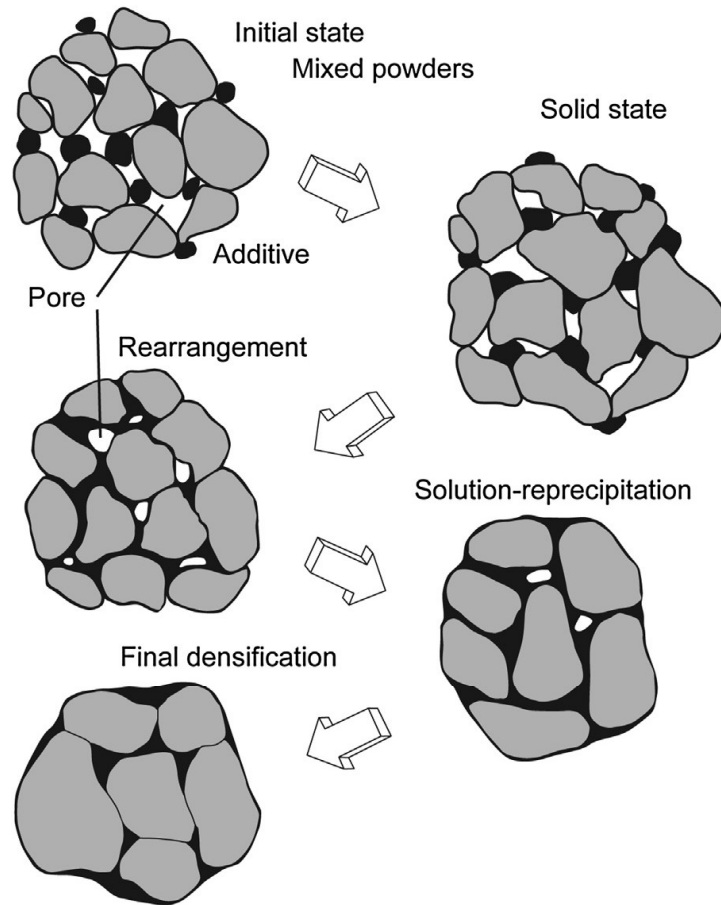


Figure 2.4: Picture of the densification process during liquid-phase sintering [22].

rial [22]. The liquid binder also spreads and wets the carbide more effectively than in the solid state. Coarsening of WC grains occurs through solution-precipitation according to Ostwald ripening, where W and C atoms diffuse through the binder from smaller to larger grains to reduce total interface area. WC grain growth is also believed to take place by means of grain boundary migration [24]. The growth of the WC grains will eventually lead to the formation of a rigid three-dimensional solid skeletal structure with liquid dispersed in the spaces between solid grains [22]. After this stage the final densification occurs slowly and it is often common to apply an external pressure which aids in closing the remaining pores. During the final stage the WC grains continue to grow.

Experimental studies on the shrinkage in WC–Co cemented carbides during sintering shows that the shrinkage is faster in W-rich alloys compared to C-rich alloys in the early stages of sintering [25, 26]. This is illustrated in Fig. 2.5, where the shrinkage and shrinkage rate is plotted for one W-rich and one C-rich alloy. It

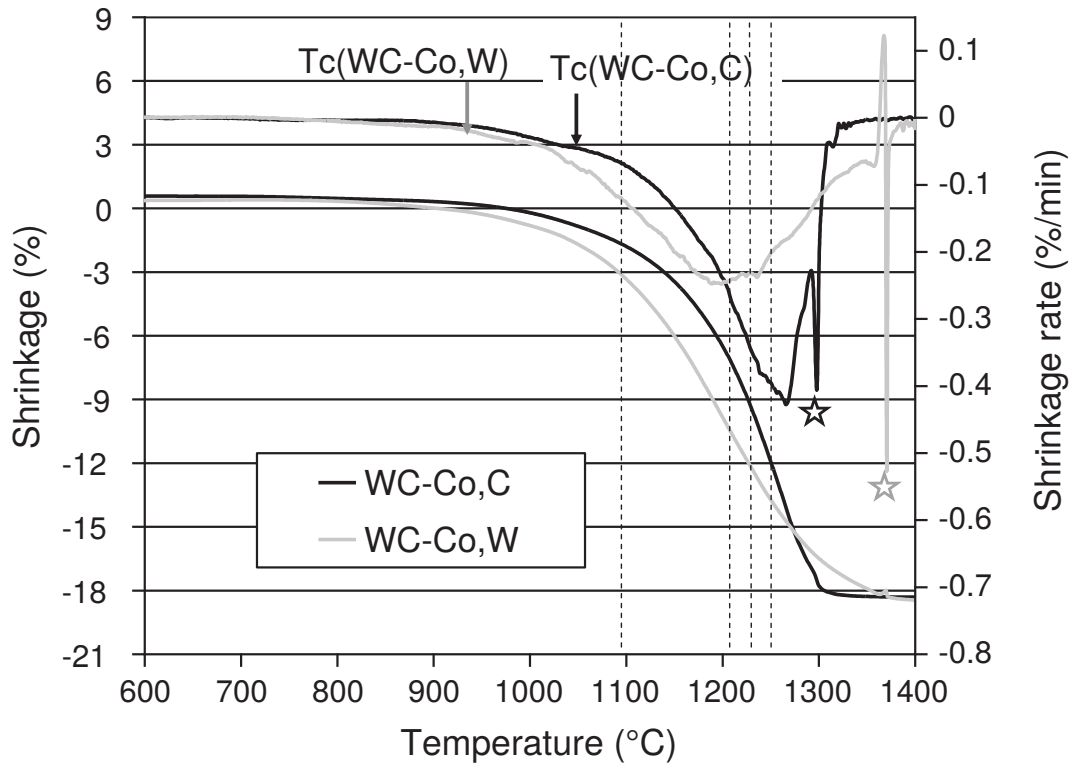


Figure 2.5: Shrinkage and shrinkage rate in W-rich (WC–Co,W) and C-rich (WC–Co,C) WC–Co cemented carbides during sintering [26]. The shrinkage is represented by the two lower curves, while the shrinkage rate is represented by the two upper curves. The stars indicate the eutectic temperatures for the two alloys.  $T_c$  marks the Curie temperature for the two alloys.

was hypothesized that the difference arises due to differences in the Curie temperature  $T_C$  of the two alloys. At the Curie temperature the magnetic state of the material goes from ordered (ferromagnetic) to disordered (paramagnetic). Further, ab-initio calculations of TiC/Co phase boundary energies in the ferromagnetic and non-magnetic states predict that the interface energy is smaller above  $T_C$ . By analogy, the WC/Co phase boundaries should behave similarly and the shrinkage should increase above  $T_C$ . Consequently, since  $T_C$  is lower in a W-rich alloy compared to a C-rich alloy, the shrinkage rate should increase earlier in the sintering in the W-rich alloy. The higher shrinkage rate for C-rich alloys at the later parts of the sintering could be the result of it having more pores left to shrink compared to the W-rich alloy.

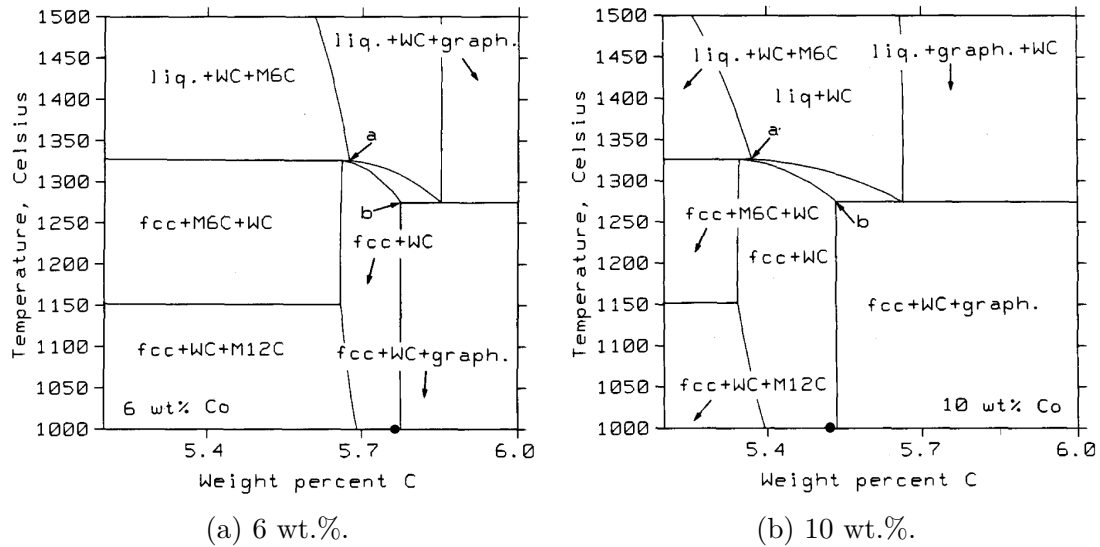


Figure 2.6: Cross sections of the phase diagrams for the W–C–Co system at 6 and 10 wt.% of binder [27]. The dots on the composition axis indicates the stoichiometric WC composition. The low and high carbon contents that defines the carbon window are marked with the letters a and b, respectively.

### 2.1.6 Controlling the phase constitution

It is crucial to control the phase constitution during the sintering cycle since the formation of unwanted phases likely will deteriorate the mechanical properties of the material [7]. In Fig. 2.6, the cross sections of the W–C–Co phase diagram at 6 and 10 wt.% of Co is shown. During sintering of WC–Co it is desired to stay within the fcc Co + WC and liquid Co + WC two-phase regions [8]. It is evident from the phase diagrams that the window of carbon contents for the fcc Co + WC two-phase region is narrow especially for the cemented carbide with low Co content. If the amount of carbon is too low, complex carbides of W–Co–C, called eta phases ( $M_6C$  and  $M_{12}C$ ), will form during sintering. These materials are characterized as brittle and will thus deteriorate the material [7]. When the carbon content is too high, uncombined carbon will form a free graphite phase which is undesirable since it undermines the mechanical strength of the material. However, the graphite phase is not considered to be as detrimental as the eta phase. This demonstrates that controlling the carbon content is a critical parameter when manufacturing cemented carbides. From Fig. 2.6 we see that a carbon content corresponding to stoichiometric WC lies within the two-phase region for both 6 and 10 wt.% of Co.

The cross sections of the W–C–Fe, W–C–Co, and W–C–Ni phase diagrams at 10 wt.% of binder is shown in Fig. 2.7. In the three cemented carbides the fcc binder + WC and liquid binder + WC two-phase regions are desired during sintering [8].

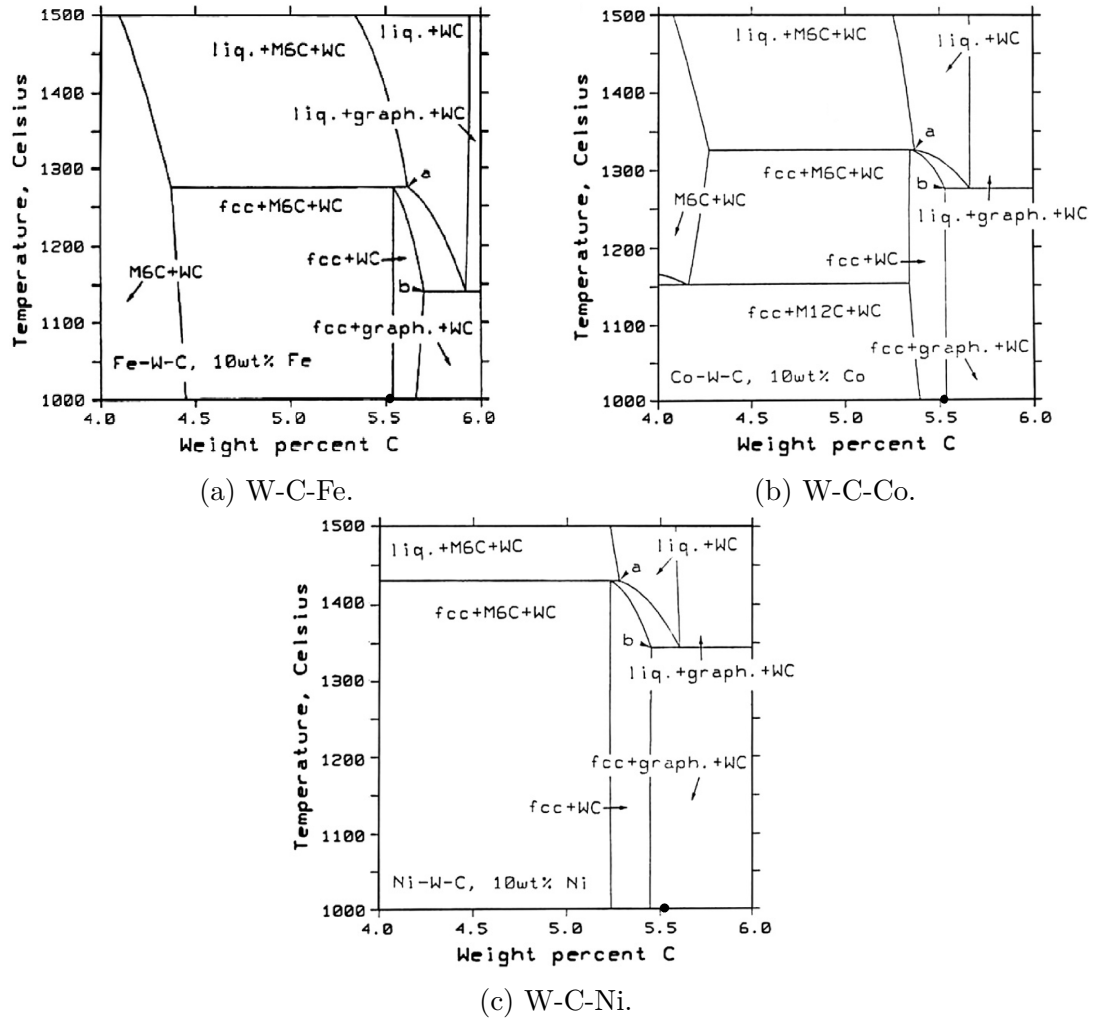


Figure 2.7: Cross sections of the phase diagrams for the three different systems, W-C-Fe, W-C-Co, and W-C-Ni, at 10 wt.% of binder [28]. The dots on the composition axis indicates the stoichiometric WC composition. The low and high carbon contents that defines the carbon windows for each alloy are marked with the letters a and b, respectively.

The phase diagrams of the three different systems are similar when comes to the phases that are present. We see that the carbon window of W-C-Ni is comparable to that of W-C-Co, however for W-C-Fe the carbon window is much narrower which complicates the sintering process. For both W-C-Fe and W-C-Ni the stoichiometric composition lies outside the desired two-phase region. In stoichiometric W-C-Fe eta phase will form upon cooling and carbon therefore have to be added to avoid formation of eta phase [8, 29]. However, in stoichiometric W-C-Ni graphite will form upon cooling which means a lower carbon content is desired [8]. Further, the higher sintering temperatures for W-C-Ni compared to Co leads to carbon pickup which may cause graphite formation [9, 29]. Additionally, the vapour pressure of Ni is high (10 times that of Co) which may lead to loss of Ni during sintering if the working pressure is not controlled properly [9].

In the DFT calculations in the appended papers we vary the chemical potential of carbon in intervals that correspond to carbon contents between the graphite and eta limits.

## Microstructure of cemented carbides

The microstructure of cemented carbides consists of faceted WC grains embedded in a matrix of binder phase [30]. This is illustrated in Fig. 3.1, where the typical microstructure of a WC–Co cemented carbide is shown. The binder phase does not completely surround the WC grains, instead, the WC grains form contacts with other WC grains and thus build up a continuous skeleton. This microstructure ensures that the high hardness of WC and the high toughness of the binder are combined which makes this a unique material of great importance.

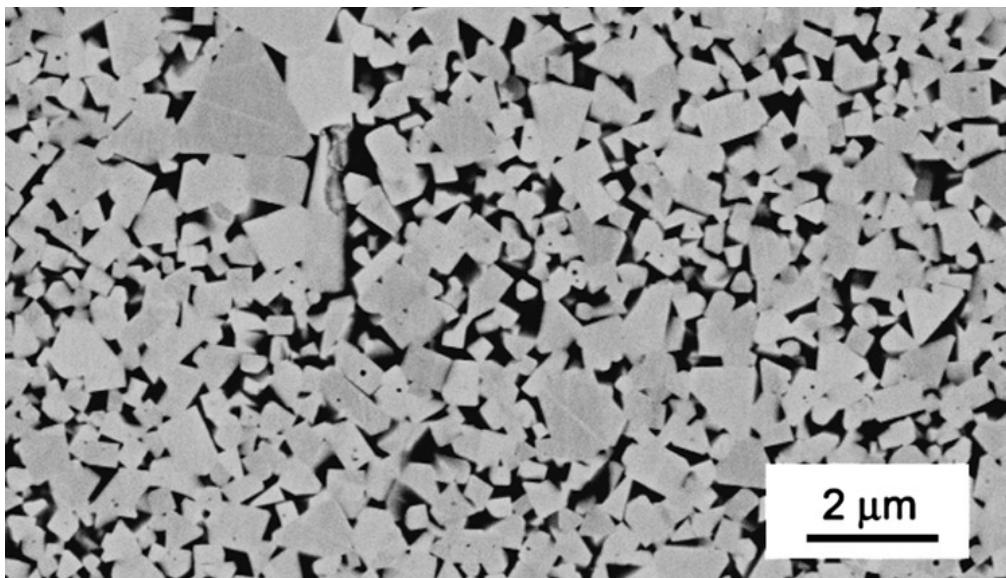


Figure 3.1: Scanning electron microscopy (SEM) micrograph of the typical microstructure of a WC–Co cemented carbide with 12 at.% Co [30]. Bright grey indicates WC and dark grey indicates Co.

### 3.1 Hard phase - Tungsten carbide

In the W-C system there are three individual carbides present:  $W_2C$ , WC, and  $\gamma$ - $WC_{1-x}$  [17, 31]. The former, tungsten semicarbide, comes in three different version, where two are hexagonal and one is orthorombic. These tungsten semicarbides only exists in thermodynamic equilibrium above 1523 K. The  $\gamma$ - $WC_{1-x}$  carbide has a rocksalt (B1) structure and is thermodynamically stable in the 2789-3058 K temperature range. The major carbide in the W-C system, and the one which is relevant in cemented carbides, is tungsten (mono)carbide (WC). WC has a simple hexagonal crystal structure with a two atom basis consisting of a W atom in  $(0, 0, 0)$  and a C atom in either  $(2/3, 1/3, 1/2)$  or  $(1/3, 2/3, 1/2)$  in terms of the hexagonal lattice vectors  $(\mathbf{a}_1, \mathbf{a}_2, \mathbf{c})$ , which are defined as

$$\mathbf{a}_1 = -\frac{a}{2}\hat{\mathbf{x}} - \frac{a\sqrt{3}}{2}\hat{\mathbf{y}} \quad (3.1)$$

$$\mathbf{a}_2 = a\hat{\mathbf{x}} \quad (3.2)$$

$$\mathbf{c} = c\hat{\mathbf{z}}. \quad (3.3)$$

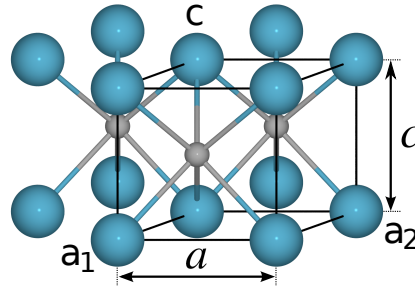


Figure 3.2: The hexagonal WC crystal structure. Large cyan coloured atoms are W and small grey atoms C. The black lines mark the primitive cell.

In Fig. 3.2, the structure and primitive cell are shown. The lattice parameters are  $a = 2.906 \text{ \AA}$  and  $c = 2.837 \text{ \AA}$ , which implies that  $c/a = 0.976$  [18]. WC exhibit no deviations from stoichiometry as it essentially contains no carbon vacancies [32]. The melting temperature of WC is 2993 K [20], which well above the relevant sintering temperatures, see Sec. 2.1. In contrast to the binder phase which dissolves appreciable amounts of WC, the WC phase dissolves very little or no amount of Co or other binder phase atoms [1]. Small amounts, below 1 at%, of additional elements such as Ta, Nb, Cr, and V can dissolve in the carbide phase [33].

The equilibrium shape of WC grains in Co is a truncated prism bounded by basal  $(0001)$  planes and prismatic  $(10\bar{1}0)$  planes which is illustrated in Fig. 3.3a. TEM

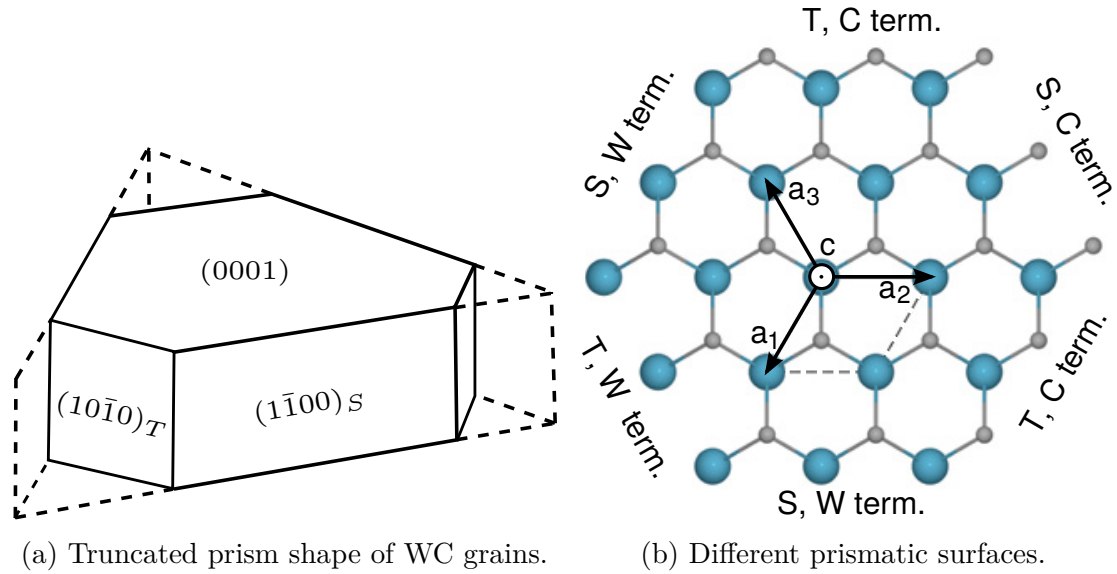


Figure 3.3: (a) Truncated prism shape of WC in cemented carbides. The prism is bounded by basal and prismatic planes. The dashed lines show the primitive cell which is also showed in Fig.3.2. Large cyan coloured atoms are W and small grey atoms C (b) Illustration of the inequivalent prismatic planes S and T seen from the [0001] direction [34].

images of real WC grains can be seen in Fig. 3.4. The truncated prism shape arises from differences in interface energies of phase boundaries with prismatic  $(10\bar{1}0)$  WC planes of different types, where the two types of prismatic surface arise due to the non-centrosymmetric crystal structure of WC [35]. They are denoted S and T [36], and are illustrated in Fig. 3.3b. The type can be determined by the number of bonds between atoms in the terminating layer and the atoms in the second layer. A prismatic surface is of type S (T) if the terminating W (C) atoms are bonded to four C (W) atoms, or if the terminating C (W) atoms are bonded to two W (C) atoms. With an increasing carbon activity the grains become less truncated. An increased carbon activity also leads to a larger WC grain size after sintering which can be seen in Fig. 3.4. The typical WC grain size is around  $1 \mu\text{m}$ .

The growth rate and thus the final grain size of WC varies for different binder phases [37]. In WC-Fe, the grain growth is inhibited and the grain size of WC is therefore smaller compared to WC-Co. In WC-Ni, on the other hand, the growth rate is larger than in WC-Co, and consequently, the final grain size is larger. This difference in WC growth rate for the three different cemented carbides is illustrated in Fig. 3.5, where microstructures of the three cemented carbides made from the same WC powder can be seen.



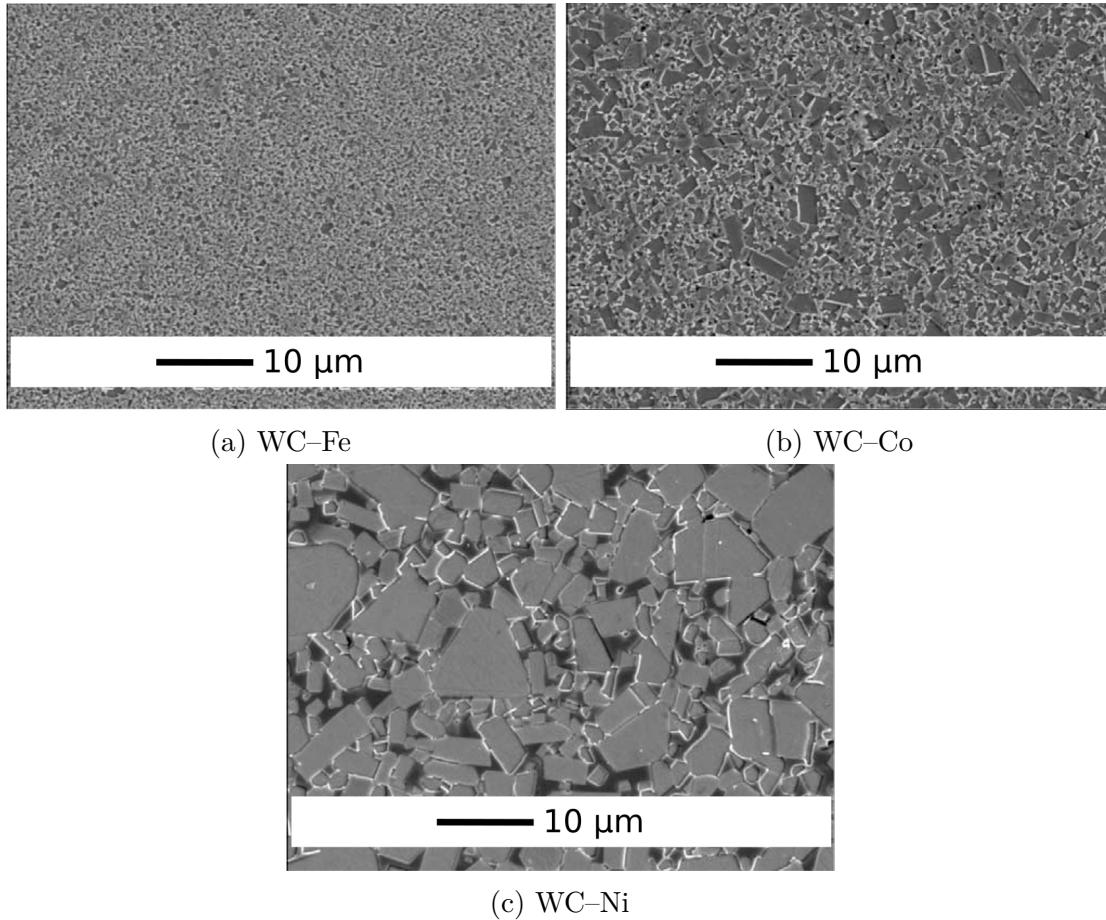


Figure 3.5: Microstructures of WC-10 wt% Co/Ni/Fe alloys, based on the same sub-micron sized WC powder [37].

concentration gradients of W are formed due to the decrease in diffusion rate of W as the temperature drops.

With the dissolved tungsten and carbon atoms the fcc phase is stabilized even at low temperatures [29, 30]. Additionally, tensile residual stresses at low temperatures probably also stabilize the fcc phase. Consequently, the fcc phase is the prominent phase of the Co binder in the cemented carbide. However, some hcp is still present due to the fcc-hcp transformation [30]. The dissolved W and C also lowers the Curie temperature of the binder [26], with a more pronounced effect in W-rich conditions compared to C-rich conditions. The eutectic temperature of WC-Co is around 1550 K [28], which is well below the melting point for pure cobalt.

The grain size of the cobalt binder phase is generally much larger than WC grains with a typical size of larger than 10  $\mu\text{m}$  for the binder compared to 1  $\mu\text{m}$  for the

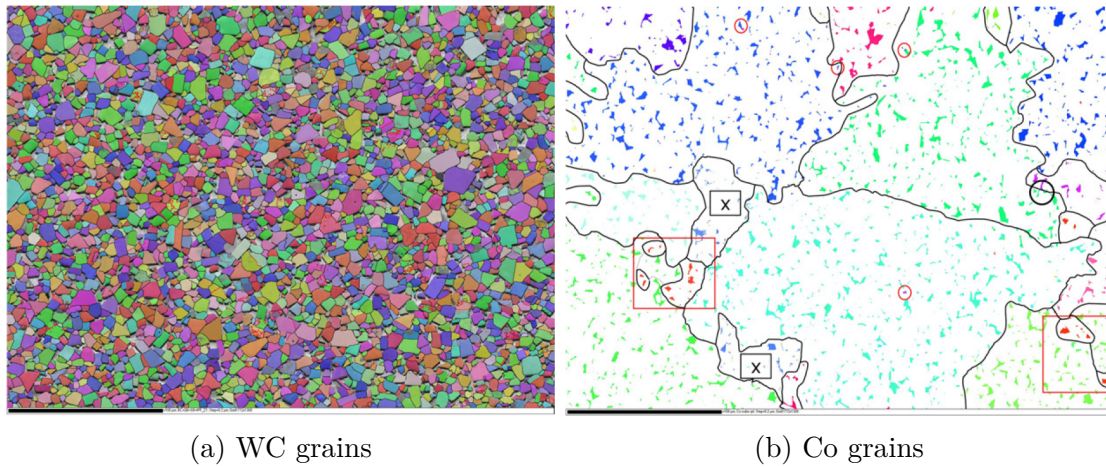


Figure 3.6: EBSD orientation maps of a WC–11Co (wt%) alloy: (a) WC phase and (b) Co phase [41]. Black lines in (b) delineate Co regions with the same orientation. The scale marker corresponds to 100  $\mu\text{m}$ .

carbide [30, 40]. However, the binder phase grains do not fill up the volume which they span, but they are rather interpenetrated by WC grains, which is illustrated in EBSD orientation maps of a WC–11Co (wt%) alloy in Fig. 3.6. Consequently, to characterize the binder phase one uses the *binder mean free path* which is a measure of the thickness of the binder pockets [30].

### 3.2.2 Nickel

The stable structure of pure nickel at ambient pressure is fcc with a lattice parameter of 3.524 Å [42, 43, 38, 44]. Nickel is ferromagnetic up to its Curie temperature of 631 K, where it turns paramagnetic [45]. The melting temperature of nickel is 1728 K [44], which is lower compared to cobalt. The fcc structure of Ni is also kept in the cemented carbide. Due to Co being by far the most used binder phase, less data on the microstructure of other binders are available [30]. The solubility of WC in the binder phase is less in WC–Ni compared to WC–Co. In contrast to WC–Co, where most Co grains are larger than the WC grains, Ni grains are found to be both small and large compared to the WC grains in WC–Ni cemented carbides. The eutectic temperature of WC–Ni is around 1620 K, which is the highest of the three studied cemented carbides.

### 3.2.3 Iron

Iron has three stable allotropes at ambient pressure called  $\alpha$ ,  $\gamma$ , and  $\delta$  [46, 38].  $\alpha$ -iron, or ferrite, has a bcc structure with lattice constant 2.866 Å and is the

stable phase up to the first transition temperature of 1184 K. Between 1184 K and 1667 K iron has an fcc phase with lattice constant 3.647 Å, which is called  $\gamma$ -iron or austenite. At 1667 K the system transform back to bcc again with a lattice parameter of 2.932 Å. This phase is called  $\delta$ -iron. The melting temperature of iron is 1811 K which is the highest of the three studied binders. The magnetic state of iron is ferromagnetic up to the Curie temperature 1043 K, above which, the material is paramagnetic [46]. Similar to cobalt the dissolved W and C atoms stabilize the fcc phase of Fe which is the predominant phase in WC–Fe cemented carbides. The solubility of W and C in the binder in WC–Fe is inferior to both WC–Co and WC–Ni [1]. Although the melting temperature for Fe is higher than both Co and Ni, the eutectic temperature of WC–Fe is only around 1420 K, which is the lowest of the three cemented carbides [8].

### 3.3 Interfaces in cemented carbides

There is a close relationship between the microstructure and the mechanical properties of cemented carbides [30]. In particular, the phase composition, phase distribution and grain size are of special importance. The phase distribution in cemented carbides are to a large extent monitored by the relative energy of interfaces [30, 47]. In the literature, there are many studies on the morphology of interfaces in WC–Co, however, the literature is scarce on similar studies for systems with alternative binders. Hence, this section will focus on interfaces in WC–Co cemented carbides.

The distribution of WC grain orientations in WC/WC grain boundaries and WC/Co phase boundaries in a WC–Co cemented carbide was analyzed by Kim *et al.* [48, 49]. To create the orientation maps, they used an orientation imaging microscopy (OIM) system incorporated in a SEM, which uses the electron backscatter diffraction (EBSD) technique, in conjunction with AFM. The orientation maps for the WC/WC grain boundaries and WC/Co phase boundaries can be seen in Fig. 3.7.

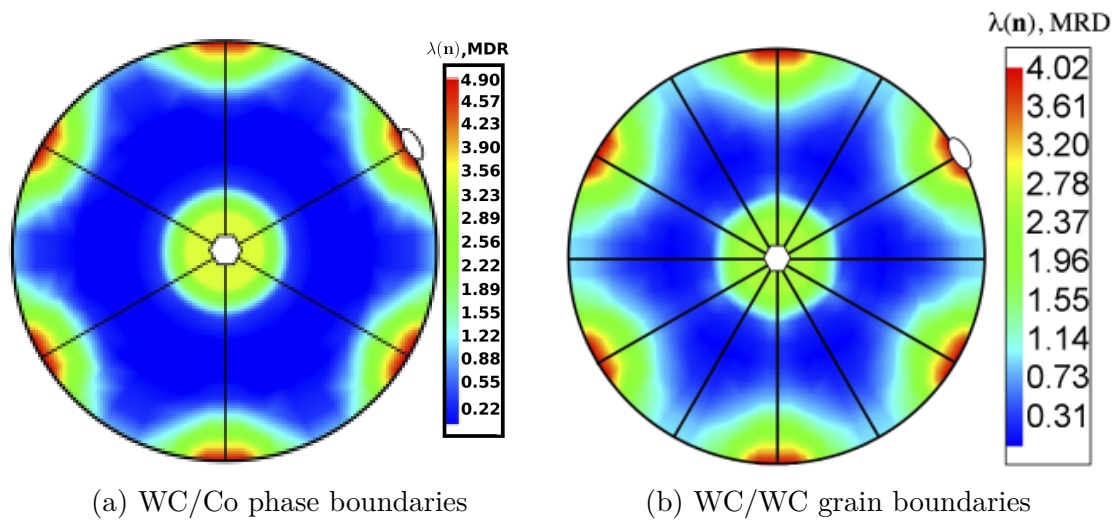


Figure 3.7: Distribution of WC grain orientations in a 12 vol% of cobalt sample for phase boundaries (a) and grain boundaries (b) [48]. The basal orientation is marked with a prism and the prismatic orientation is marked with an oval.

The distributions are plotted in multiples of a random distribution (MRD) for a hexagonal crystal. This means that orientations with areas greater than expected in a random distribution have values greater than one, and orientations with areas less than expected in a random distribution have values less than one. The figures are stereograms of a 3D distribution with the basal direction in the center and the prismatic orientation on the periphery, which is marked by a prism and ovals respectively. The peaks for the basal and prismatic orientations clearly show that these are the two most common WC planes in the WC–Co microstructure. Using a  $5^\circ$  tolerance angle, Kim *et al.* found that approximately 80% of the WC/Co boundaries and 60 % of the WC/WC grain boundaries can be classified as having either one basal or one prismatic WC boundary plane.

### 3.3.1 WC/WC grain boundaries

The WC/WC grain boundaries are important for the material strength as the WC grains builds up a continuous skeleton in the cemented carbide [30]. Experiments show that a majority of crack paths in WC–Co cemented carbides consists of broken up grain boundaries [50]. This demonstrates the importance of the strength of WC/WC grain boundaries when it comes to the mechanical strength of the material. Further, in experiments where the Co phase was etched out from the WC–Co cemented carbide, it was found that the etched material was stronger but also more brittle compared to the cemented carbide above  $1100^\circ\text{C}$  in three-point bending tests [51]. This indicates that the presence of the binder phase weakens the material

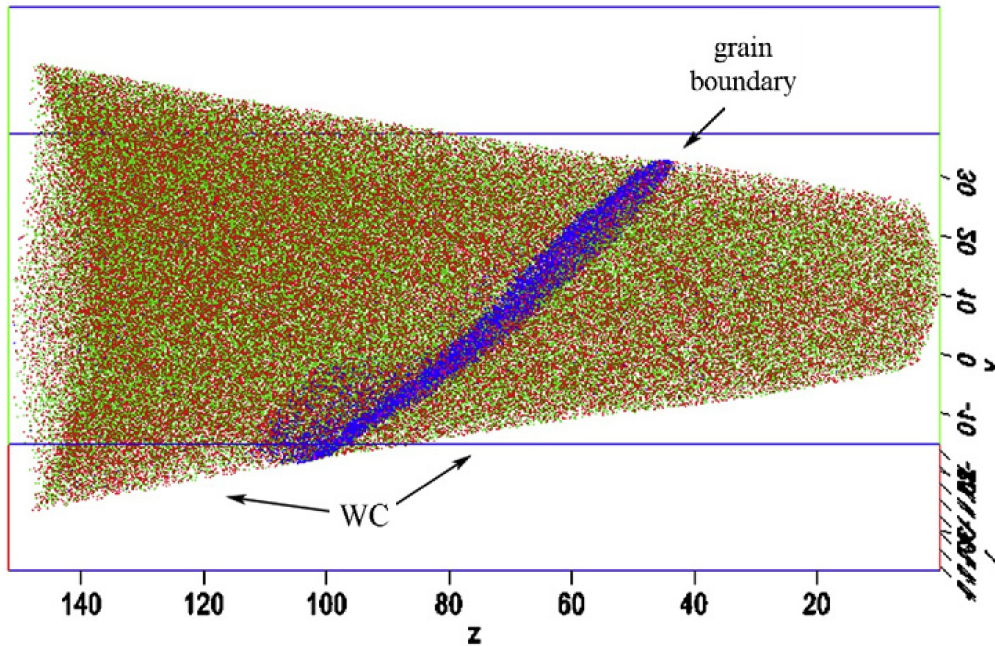


Figure 3.8: APT reconstruction of a WC/WC grain boundary in a WC–TiC–Co material [58]. Green dots = W atoms, red = C, blue = Co, pink = Ti.

at higher temperatures. It is believed that this reduction in strength is due to WC/WC grain boundaries are being infiltrated by binder phase and thus facilitating grain boundary sliding which is the dominating plastic deformation mechanism at high temperatures [52, 51, 53].

In experiments of the growth of WC grains during sintering it was observed that WC/WC grain boundaries are typically curved at lower temperatures but straighten out at higher temperatures and for longer sintering times [54]. It has also been demonstrated both experimentally and from first principles calculations that grain boundaries in WC–Co generally contain roughly 0.5 monolayer of segregated Co atoms [55, 56, 57, 58, 34]. This is demonstrated in an atom probe tomography (APT) reconstruction of a WC/WC grain boundary in a WC–TiC–Co material seen in Fig. 3.8. When additions is used in cemented carbides, such as TiC, NbC and ZrC, the metal atoms are in many cases found to segregate to WC/WC grain boundaries [57, 58].

Grain boundaries are commonly characterized by the coincidence site lattice and the misorientation of the adjoining crystals [59]. The coincidence site lattice index,  $\Sigma$ , is defined as follows: If the two adjoining grains are translated such that the lattices coincide, then  $\Sigma$  is the inverse of the fraction of coincident lattice points [60, 61]. Since the ratio  $c/a = 0.976$  for WC is close to 1, it has the possibility

of forming many low  $\Sigma$  grain boundaries in the  $c/a = 1$  approximation [50]. The most studied grain boundary in literature is the  $\Sigma = 2$  twist grain boundary which is formed upon a rotation of  $90^\circ$  around a common  $[10\bar{1}0]$  axis [62], see Fig. 3.9. It has been studied experimentally in Refs [63, 64, 65, 66, 54, 67] and using first principles in [68, 69]. The interface energy of the  $\Sigma = 2$  twist grain boundary is low due to the preserved bulk like coordination across most of the interface [68, 70]. The special  $\Sigma = 2$  twist grain boundary in WC–Co have been found, both from experiments and modelling, to have no segregated Co atoms [63, 68]. Further, the  $\Sigma = 2$  twist grain boundaries are, due to their stability, believed to originate from the powder. This is supported by experiments where the fraction of  $\Sigma = 2$  twist grain boundaries are shown to decrease during sintering when small grains dissolve and larger grow [54, 65, 66]. Also, TEM investigations on clusters in the powder and sintered material indicate that  $\Sigma = 2$  twist grain boundaries arise from the powder [64].

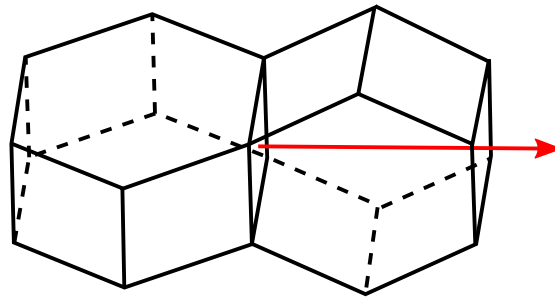


Figure 3.9: Simple sketch of the pure twist  $\Sigma = 2$  grain boundary arising from a  $90^\circ$  rotation around a common prismatic  $[10\bar{1}0]$  axis (red arrow). The interface relation is  $(10\bar{1}0) \parallel (10\bar{1}0)$ ,  $[0001] \parallel [1\bar{2}10]$ .

The population of misorientations (rotations) for grain boundaries in WC–Co was measured by Kim *et al.* [48] and the results are displayed in Fig. 3.10. A clear peak at  $90^\circ$  is seen which was identified as the  $\Sigma = 2$  twist grain boundary. There is also a clear peak at around  $30^\circ$ , which correspond to rotations around the  $[0001]$  axis resulting in  $\Sigma = 13$  [30]. In most cases, the grain boundary is bound by two  $(0001)$  planes (twist boundary), however, grain boundaries with  $(10\bar{1}0)$  and  $(1\bar{2}10)$  planes (asymmetric tilt boundary) also occur. In the study they found that the  $90^\circ/[10\bar{1}0]$  grain boundaries make up 11-14 % of the total grain boundary population, whereas the same figure for the  $30^\circ/[0001]$  grain boundaries was 2-3 %. Additionally, grain boundaries with a misorientation of  $90^\circ$  around the  $[1\bar{2}10]$  axis were more common than the expected value from a random distribution. These grain boundaries are mostly bound by one basal and one prismatic WC plane and the coincidence site

lattice index for this grain boundary is  $\Sigma = 97$  [66]. As mentioned previously in Sec. 3.3, about 60 % of the grain boundaries in WC–Co can be classified as having either one basal or one prismatic WC boundary plane [48].

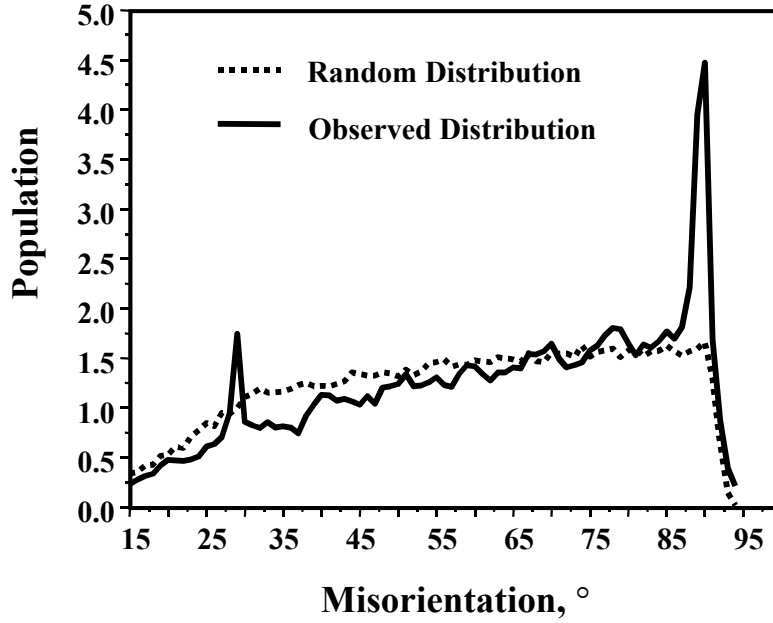


Figure 3.10: Grain boundary population of WC crystals and random objects as a function of misorientation angle [49].

### 3.3.2 WC/Co phase boundaries

The interface energies of the phase boundaries in cemented carbides are important for the behaviour during sintering, especially when it comes to grain growth [30]. It is the energy of the phase boundaries that determine the morphology of the WC grains in cemented carbides [35]. Generally, WC/Co phase boundaries are planar and sharp locally [71]. In WC–Co with high carbon contents the WC grains are perfectly sharp and faceted. However, for low carbon contents, the grains have slightly rounded corners and steps are found on the WC/Co phase boundaries. To illustrate this, TEM images of WC/Co Phase boundaries in a C-rich and a W-rich WC–Co cemented carbide are shown in Fig. 3.11.

During the solidification of the cobalt binder phase in WC–Co after liquid-phase sintering the Co grains are allowed to grow without any preference to orientations of the surrounding WC grains [72]. There is thus no orientation structure of general WC/Co phase boundaries similar to the one observed for WC/WC grain boundaries. However, as mentioned in Sec. 3.3, about 80 % of the phase boundaries in WC–Co

can be classified as having either one basal or one prismatic WC boundary plane [48]. Further, general WC/Co phase boundaries have been found to have a thin, only two atomic rows,  $WC_{1-x}$  cubic layer at the interface [72]. Similarly, in VC doped WC–Co cemented carbides,  $(V,W)C_{1-x}$  cubic layers are found in the phase boundaries [73, 74], which also is supported by modelling [75, 76]. Experimental studies on cobalt inclusions in WC grains reported phase boundaries bounded by WC(0001) planes and Co(111) planes [77, 78]. Similarly, in small Co pools, phase boundaries bounded by WC(0001) and Co(111) or Co(001) were reported [72]. In solid-state sintered cemented carbides these special orientations are frequently found [25].

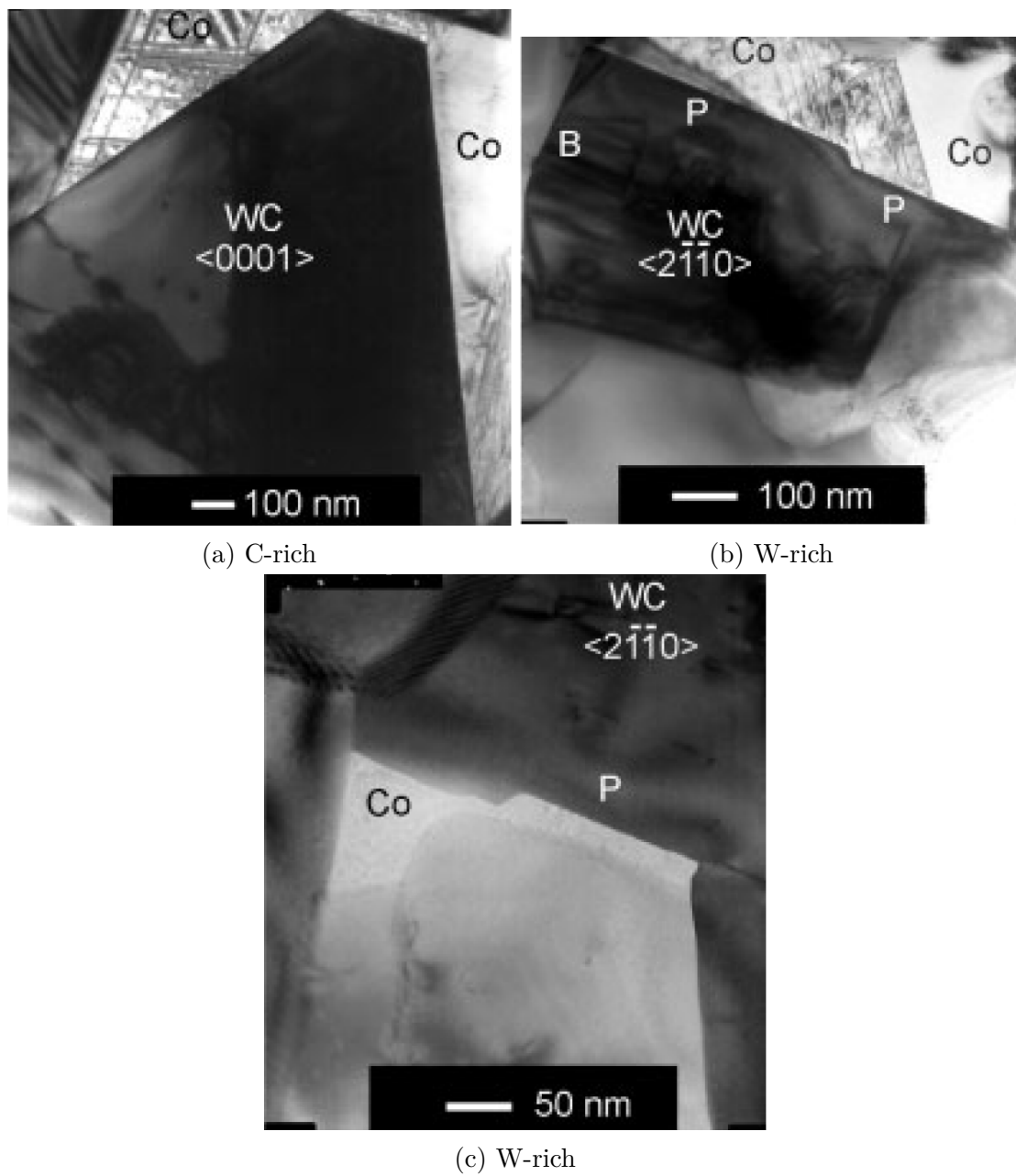


Figure 3.11: TEM images of a perfectly faceted WC grain and sharp WC/Co phase boundaries in a C-rich WC–Co cemented carbide (a), and stepped WC/Co phase boundaries in a W-rich WC–Co cemented carbide (b,c) [71].



## Model geometries of interfaces in cemented carbides

In Sec. 3.3, experimental findings from the literature regarding the morphology of WC/Co phase boundaries and WC/WC grain boundaries in WC–Co cemented carbides was presented. The most important finding was that 80% of WC/Co phase boundaries and 60% of WC/WC grain boundaries can be classified as having a boundary plane that is either basal or prismatic. We use this information to construct model WC/WC grain boundaries, WC/binder phase boundaries, WC surfaces, and binder surfaces which are appropriate for DFT calculations. The binder/binder grain boundaries are omitted since, in WC–Co cemented carbides, Co grains generally are much larger than WC grains [40, 30] and the Co/Co grain boundaries therefore do not contribute as much to the properties of the final material as do the other interfaces. Since DFT calculations are quite computationally heavy, rather small repeating unit cells (<100 atoms) are required. The model WC/binder phase boundaries, WC surfaces, and binder surfaces are constructed based on WC planes in the model grain boundaries.

### 4.1 WC/WC grain boundaries

In order to get small repeating unit cells for the model grain boundaries, a small coincidence site lattice index  $\Sigma$  (defined in Sec. 3.3) is required. As stated in Sec. 3.3.1, the  $\Sigma = 2$  twist grain boundary is the most common grain boundary and it associated with very low interfacial energy. However, as the  $\Sigma = 2$  twist grain boundaries originate already from the powder [64] they do not play an essential role in the formation of the final continuous skeleton of hard WC grains.

They are therefore not an appropriate choice of model for a more general grain boundary relevant for studying quantities, such as the mechanical strength of the material, which are dependent on the WC skeleton. The second most common grain boundary is the  $30^\circ/[0001]$  grain boundary, most frequently bound by two basal planes, which has a coincidence site lattice index of  $\Sigma = 13$  [48, 30]. Due, to its rather high  $\Sigma$ -value it requires quite large repeating unit cells which makes it inappropriate for DFT calculations. The third most common grain boundary was found to be  $90^\circ/[\bar{1}\bar{2}10]$  which were mostly bound by one basal and one prismatic WC plane. However, since the coincidence site lattice index for this grain boundary is very high,  $\Sigma = 97$ , it is not appropriate for DFT calculations. We therefore have to look for other grain misorientations that give rise to low  $\Sigma$ -values.

The two lowest possible  $\Sigma$ -values are  $\Sigma = 2$  and  $\Sigma = 4$  which are the results of  $90^\circ/[10\bar{1}0]$  and  $60^\circ/[\bar{1}\bar{2}10]$ , respectively. Instead of the pure twist  $\Sigma = 2$  grain boundary we therefore choose the  $\Sigma = 2$  tilt grain boundary, bound by one basal and one  $(\bar{1}\bar{2}10)$  plane, as a model grain boundary. The basal boundary planes can be seen in Figs 4.1a and 4.2a, and the  $(\bar{1}\bar{2}10)$  boundary planes can be seen in Figs 4.1c and 4.2c. This type of grain boundary has been observed experimentally in Ref. [79]. We also choose the  $60^\circ/[\bar{1}\bar{2}10]$   $\Sigma = 4$  tilt grain boundary bound by one prismatic and one  $(10\bar{1}2)$  plane as a model grain boundary. The prismatic boundary planes can be seen in Figs 4.1b and 4.2b, and the  $(10\bar{1}2)$  boundary planes is seen in Figs 4.1d and 4.2d. Experimental findings indicating the presence of this  $\Sigma = 4$  grain boundary in cemented carbides is found in Ref. [80]. This choice of model grain boundaries ensures that we end up with small repeating unit cells as well as having grain boundaries bound by at least one basal or one prismatic WC plane.

We use the  $c/a = 1$  approximation to choose our model grain boundaries. However, in the DFT calculations we fix the simulation cells in the interface plane but use vacuum regions at the two remaining WC planes not in the grain boundary. This means that the systems are allowed to relax in the direction perpendicular to the interfaces. Since the orientation of the grains in a grain boundary are different they will relax differently. To solve this, we vary the value of  $a = c$  and choose the value where the two grains relax such that the energy of a WC unit is equal in both grains. The two grains are thus in equilibrium with each other and we use the strained WC phase as reservoir for the grain boundary system. In the phase boundary systems the binder phases are strained in order to match with WC, and in this case the strained energy is used as reservoir energy for the binder phase.

### 4.1.1 $\Sigma = 2$ model grain boundaries

Due to the lack of mirror symmetry of the prismatic planes, see Sec. 3.1, it is possible to construct two different  $\Sigma = 2$  tilt grain boundaries that are not related by an interface translation. By rotating one of the grains  $180^\circ$  around an axis

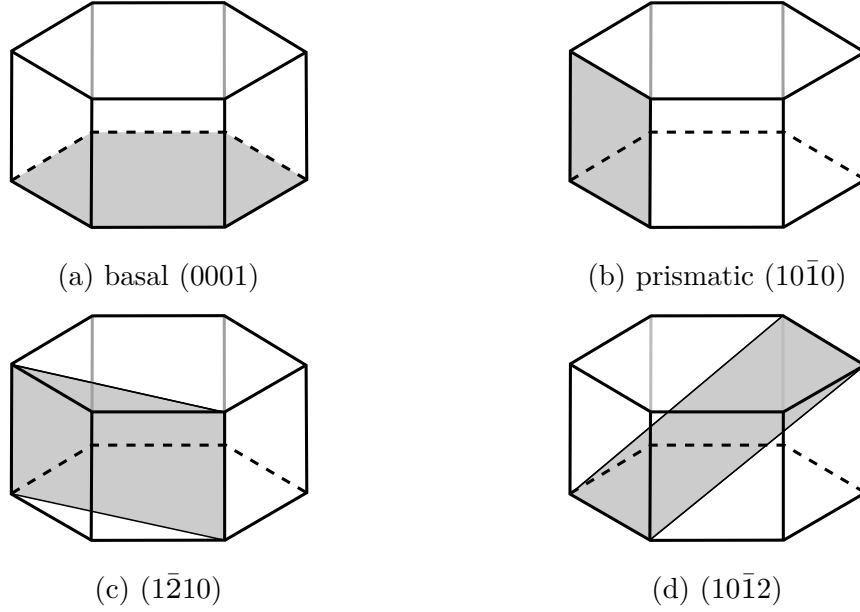


Figure 4.1: Low index WC planes used in the two  $\Sigma = 2$  and four  $\Sigma = 4$  grain boundaries. The hexagonal prism correspond to the structure in Fig. 3.2

perpendicular to the prismatic axis (e.g. the basal or  $[1\bar{2}10]$  axes), the lattice is equivalent, however, the positions of the C atoms has changed. This means that prismatic axis of the rotated grain has changed from type S (T) to type T (S). See Sec. 3.1 for more details regarding S and T type. The interface relations for the two  $\Sigma = 2$  tilt grain boundaries are

$$\Sigma = 2_1 : (0001) \parallel (1\bar{2}10), \quad [10\bar{1}0] \parallel [10\bar{1}0], \quad (4.1)$$

$$\Sigma = 2_2 : (0001) \parallel (1\bar{2}10), \quad [\bar{1}010] \parallel [10\bar{1}0]. \quad (4.2)$$

The basal plane can be either W or C terminated, while the mixed  $(1\bar{2}10)$  is invariant, up to a translation, under the addition or removal of atomic layers. The fully relaxed  $\Sigma = 2_1$  grain boundary can be seen in Fig.4.3a.

#### 4.1.2 $\Sigma = 4$ model grain boundaries

Both the  $(10\bar{1}0)$  and  $(10\bar{1}2)$  planes lack mirror symmetry and should therefore be marked with the subscript S or T denoting their type. By changing the types of the WC planes it is possible to construct four different  $\Sigma = 4$  tilt grain boundaries that are not related by an interface translation. The type is changed upon a rotation of  $180^\circ$  around an axis perpendicular to the prismatic axis. The interface relations

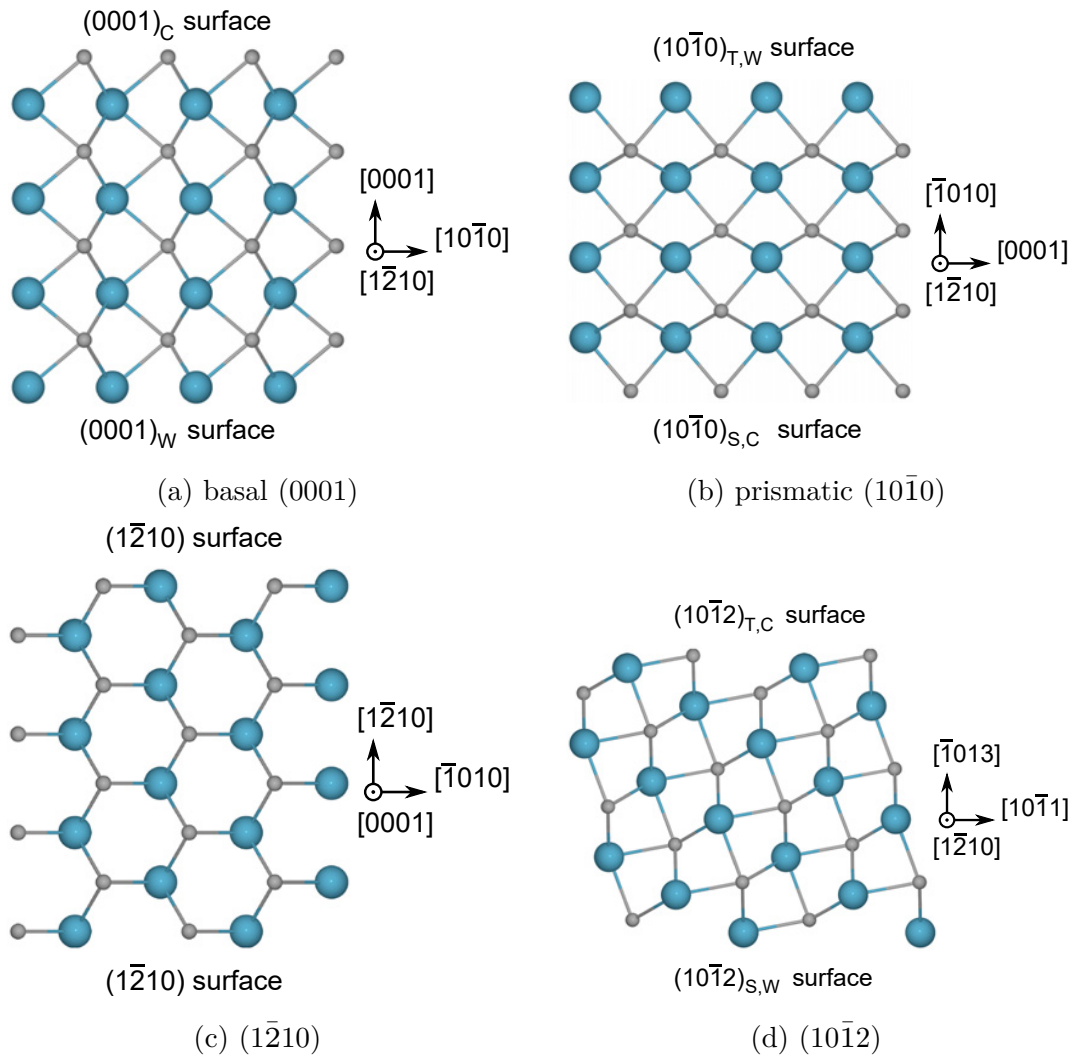


Figure 4.2: Unrelaxed atomic structures of the low-index WC surfaces which are shown schematically in figure Fig. 4.1 [34]. Large cyan coloured atoms are W and small grey atoms are C.

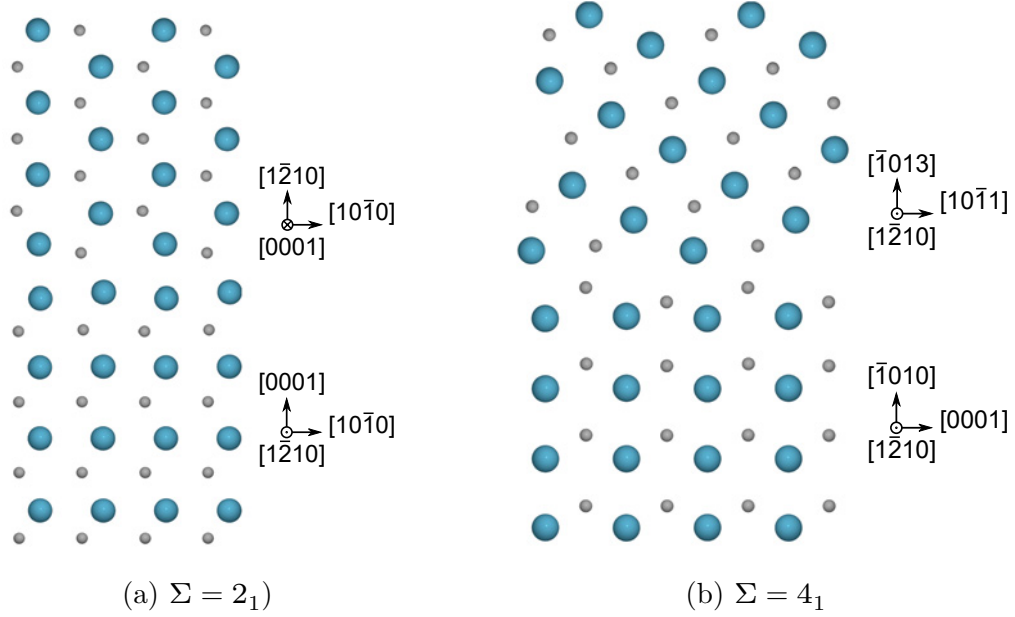


Figure 4.3: Geometries of the  $\Sigma = 2_1$  and  $\Sigma = 4_1$  grain boundaries [34]. Large cyan coloured atoms are W and small grey atoms are C. The figure shows the actual positions of the atoms in the fully relaxed minimum energy structures.

for the four  $\Sigma = 4$  tilt grain boundaries are

$$\Sigma = 4_1 : (\bar{1}010)_T \parallel (\bar{1}012)_S, \quad [0001] \parallel [10\bar{1}1], \quad (4.3)$$

$$\Sigma = 4_2 : (\bar{1}010)_T \parallel (\bar{1}012)_T, \quad [0001] \parallel [\bar{1}01\bar{1}], \quad (4.4)$$

$$\Sigma = 4_3 : (\bar{1}010)_S \parallel (\bar{1}012)_S, \quad [000\bar{1}] \parallel [10\bar{1}1], \quad (4.5)$$

$$\Sigma = 4_4 : (\bar{1}010)_S \parallel (\bar{1}012)_T, \quad [000\bar{1}] \parallel [\bar{1}01\bar{1}]. \quad (4.6)$$

In this way the  $\Sigma = 4_1$  and  $\Sigma = 4_4$  boundaries are  $60^\circ/[1\bar{2}10]$  tilt grain boundaries [62, 64], while the  $\Sigma = 4_2$  and  $\Sigma = 4_3$  boundaries correspond to  $240^\circ/[1\bar{2}10]$  grain boundaries. Both the  $(10\bar{1}0)$  and  $(10\bar{1}2)$  planes can be either W or C terminated which means that there are four different termination possibilities for each  $\Sigma = 4$  tilt grain boundary. We denote the termination of a WC plane by an additional subscript such that  $(10\bar{1}0)_{S,W}$  is a W terminated prismatic plane of type S. The fully relaxed  $\Sigma = 4_1$  grain boundary can be seen in Fig. 4.3b.

## 4.2 WC/Binder phase boundaries

The model phase boundaries are created by matching the WC planes in the model  $\Sigma = 2$  and  $\Sigma = 4$  grain boundaries with fcc binder. In order for DFT calculations

to be feasible, the phase boundaries need to have a small repeating unit cells. However, this comes at the expense of straining the binder phases. The (0001) and ( $\bar{1}\bar{2}10$ ) planes have matching repeating unit cells and are both matched with the fcc(111) plane to achieve minimal strain according to

$$(0001) \parallel (111), \quad [2\bar{1}\bar{1}0] \parallel [\bar{1}\bar{1}\bar{2}], \quad (4.7)$$

$$(\bar{1}\bar{2}10) \parallel (111), \quad [000\bar{1}] \parallel [\bar{1}\bar{1}\bar{2}]. \quad (4.8)$$

The ( $10\bar{1}0$ ) and ( $10\bar{1}2$ ) plane are matched with the fcc(001) plane instead, and the interface relations are

$$(10\bar{1}0) \parallel (001), \quad [0001] \parallel [3\bar{1}0], \quad (4.9)$$

$$(10\bar{1}2) \parallel (001), \quad [\bar{1}011] \parallel [3\bar{1}0]. \quad (4.10)$$

In the case of the (0001), ( $10\bar{1}0$ ) and ( $10\bar{1}2$ ) planes the termination can be either W and C, and the ( $10\bar{1}0$ ) and ( $10\bar{1}2$ ) planes have either type S or T. We end up with six unique model phase boundaries if we include the types S and T. The strain in the binder phases are on the order of 5%.

### 4.3 Surfaces

Similar to the phase boundaries we take the WC planes from six model grain boundaries and make model WC surface systems. If the type of the ( $10\bar{1}0$ ) and ( $10\bar{1}2$ ) planes are included we end up with 6 unique model WC surfaces: (0001), ( $\bar{1}\bar{2}10$ ), ( $10\bar{1}0$ )<sub>S</sub>, ( $10\bar{1}0$ )<sub>T</sub>, ( $10\bar{1}2$ )<sub>S</sub>, and ( $10\bar{1}2$ )<sub>T</sub>. These are shown in Fig. 4.2. The planes of the binder phase in the phase boundaries are also used as model binder surfaces: fcc(111) and fcc(001).

### 4.4 Adsorption and segregation

The local chemistry of interfaces are important for thermodynamic properties such as the wettability [81]. In order to investigate effects from changes in the local chemistry of the interfaces, we model segregation of binder phase atoms to WC/WC grain boundaries and WC/binder phase boundaries, and adsorption of binder phase atoms to WC surfaces. This is done by systematically replacing W and C atoms in the vicinity of the interface for binder phase atoms. In the (0001), ( $\bar{1}\bar{2}10$ ), and ( $10\bar{1}0$ ) planes the topmost layer is considered for substitution, while for the more corrugated ( $10\bar{1}2$ ) plane, the two topmost layers are considered. The substitutional sites for one WC surface, two WC/WC grain boundaries and one WC/M phase boundary is seen in Fig. 4.4.

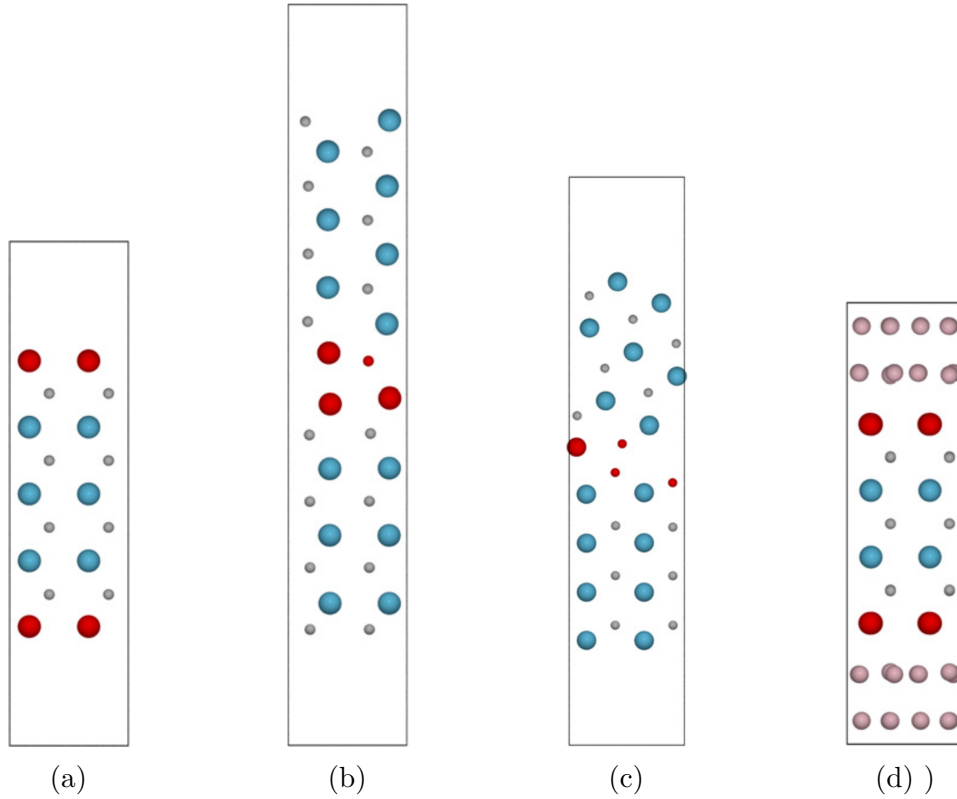


Figure 4.4: Substitutional sites at a (0001) WC surface (a), in a  $\Sigma = 2_1$  grain boundary (b), in a  $\Sigma = 4_1$  grain boundary (c), and in a (0001)||{(111) phase boundary (d) [34]. Large cyan coloured atoms are W, small grey atoms are C, medium sized pink atoms are binder phase atoms, and the red atoms mark the substitutional sites. These are the actual simulation cells used in the appended papers.

In a previous study in Ref. [34], all possible terminations of the WC planes were tested for all model interfaces in WC–Co in order to minimize the interface energy. Additionally, all substitutions that corresponded to 0.5 or 1 monolayer (ML) proportion, was investigated. The minimization also included the effect from the chemical potential of carbon  $\mu_C$  (carbon activity), which in some cases resulted in different optimal configurations depending on the value of  $\mu_C$ . In the two appended papers, the same exhaustive search for the optimal configurations for the WC–Fe and WC–Ni cemented carbides was not performed. Instead, the configurations in WC–Co which gave minimum energies for 0 (clean), 0.5 and 1 ML of substituted Co, respectively, are used. This is motivated by the similarity of the three binders.



# Thermodynamics of interfaces

Thermodynamics of interfaces in cemented carbides determine to a large degree the microstructure after sintering, which in turn determine the mechanical properties of the material [30, 47]. The two appended papers, both deal with aspects of interfacial energetics in cemented carbides.

## 5.1 Interface free energy

The fundamental quantity related to the creation of an interface is the interface free energy,  $\gamma$  [59]. To define  $\gamma$ , we must first define the interface system rigorously. Let us consider two phases which are in contact along a planar interface of area  $A$ . The interface system is in equilibrium with reservoirs which provide the system with atoms. The entire system, i. e. the two phases, the dividing interface and the reservoirs, are held at constant temperature  $T$ , pressure  $P$  and chemical potential  $\mu_i$  for each of the components. Additionally, the two adjoining bulk phases are assumed to be large in comparison with the interface system. By using a combination of the first and second laws of thermodynamics, the change in total energy due to a reversible change of the interface system may be written as

$$dE = TdS - PdV + \sum_{i=1}^C \mu_i dN_i + \gamma dA, \quad (5.1)$$

where  $S$  is the entropy,  $V$  the volume of the entire interface system,  $C$  the number of components and  $N_i$  the number of atoms of component  $i$ . This is analogous to the expression for a bulk system, apart from the last term  $\gamma dA$ , which is added to account for the change in total energy associated with a change in area of the

interface. Directly from Eq. (5.1) we get

$$\gamma = \left[ \frac{\partial E}{\partial A} \right]_{S, V, N_i}, \quad (5.2)$$

which means that the interface free energy is defined as the change in total energy of the interface system per unit increase in interface area, at constant  $S$ ,  $T$ , and  $N_i$ . However, it turns out that relating  $\gamma$  to Gibbs energy  $G$  gives the most useful expressions for calculations using DFT. If we integrate Eq. (5.1), we obtain

$$E = TS - PV + \sum_{i=1}^C \mu_i N_i + \gamma A, \quad (5.3)$$

which can be combined with the definition for  $G$

$$G = E + PV - TS \quad (5.4)$$

to get

$$\gamma = \frac{1}{A} \left[ G - \sum_{i=1}^C \mu_i N_i \right]. \quad (5.5)$$

From Eqs. (5.3) and (5.4) we see that if the atoms were to be accumulated into separate bulk phases ( $A=0$ ), then

$$G = \sum_{i=1}^C \mu_i N_i, \quad (5.6)$$

which means that  $\gamma$  is the excess Gibbs energy per unit interfacial area due to the presence of the interface.

### 5.1.1 Implementation in DFT

To get the value of  $\gamma$  using Eq. (5.5), differences in free energies need to be calculated. This is, however, difficult as DFT is a theory that predicts total energies of isolated systems and approximations therefore have to be applied. In this thesis we do not attempt to calculate accurate free energies where for example the contributions from entropy and vibrations have to be accounted for. Instead, we approximate Gibbs free energy by the total energy from DFT,  $G \approx E$ , and disregard any temperature effects. We motivate this by noting that when calculating interfacial energies, the temperature dependent terms cancel to a large degree [82, 83]. We may therefore also call  $\gamma$  the interface energy, rather than the interface free energy.

This means that apart from changing  $G$  for  $E$  in Eq. (5.5) we also have to replace the chemical potentials,  $\mu_i$ , with the total energies per atom in the respective reservoir bulk states. If we now consider the calculation of a WC/M phase boundary energy, where M denotes the binder phase (Fe/Co/Ni), we rewrite Eq. (5.5) into the approximate

$$\gamma = \frac{1}{A} \left[ E - \mu_{\text{W}} N_{\text{W}} - \mu_{\text{C}} N_{\text{C}} - \mu_{\text{M}} N_{\text{M}} \right]. \quad (5.7)$$

In this phase boundary, the adjoining bulk phases WC and M acts as reservoirs for the interface. Consequently, all W and C atoms are considered to be in equilibrium with stoichiometric WC and all M atoms in equilibrium with fcc M. If we use the approximation  $G \approx E$ , we therefore get

$$\mu_{\text{W}} + \mu_{\text{C}} = E_{\text{WC}}, \quad (5.8)$$

where  $E_{\text{WC}}$  is the total energy per formula unit of the WC bulk structure, and

$$\mu_{\text{M}} = E_{\text{M}}, \quad (5.9)$$

where  $E_{\text{M}}$  is the total energy per M atom in the M bulk fcc structure.

Eqs. (5.7) to (5.9) are sufficient for the calculations of the phase boundary with the (1210) WC plane since then  $N_{\text{W}} = N_{\text{C}} = N_{\text{WC}}$  and, consequently,

$$\gamma = \frac{1}{A} \left[ E - E_{\text{WC}} N_{\text{WC}} - E_{\text{M}} N_{\text{M}} \right]. \quad (5.10)$$

However, for the other phase boundaries the interface is not stoichiometric, i.e.  $N_{\text{W}} \neq N_{\text{C}}$ , and we therefore have to find separate values of  $\mu_{\text{W}}$  and  $\mu_{\text{C}}$ . It is here the chemical potential of C (or carbon activity) enters into the calculations. In order to calculate separate values of  $\mu_{\text{W}}$  and  $\mu_{\text{C}}$ , we need another phase, with which W and C are in equilibrium. If we recall the section about the phase constitution in cemented carbides (Sec. 2.1.6), there are two limits for the carbon activity for the desired WC + fcc M two-phase region. In the low carbon (eta) limit the complex  $\eta$ -phase carbides are formed while in the high carbon (graphite) limit graphite is formed in the material. We calculate the chemical potential of C in these two limits to get the range of  $\mu_{\text{C}}$  which is relevant in the cemented carbides. The value of  $\mu_{\text{W}}$  can then be calculated from Eq. (5.8), and interface energies of non-stoichiometric interfaces, dependent on  $\mu_{\text{C}}$ , can be calculated using Eq. (5.7).

In the case of graphite we do not make a direct DFT calculation. Instead, we calculate the total energy per atom in diamond and subtract the enthalpy difference to graphite taken from the literature in Ref. [84]. This is motivated by the higher accuracy for diamond compared to graphite with the PBE functional.

In the eta limit, there are two relevant phases (cf. Fig. 2.7)  $M_{12}C$  and  $M_6C$ . Here  $M$ , denotes a mixture of W and binder phase atoms. In WC–Co, we calculate the value for  $\mu_C$  in the  $M_{12}C$  and  $M_6C$  phases by replacing Mo atoms for W atoms in the  $Co_6Mo_6C$  and  $Co_6Mo_6C_2$  structures in Ref. [85], respectively. In WC–Ni and WC–Fe, Co is also replaced with the corresponding binder. We may then extract  $\mu_C$  from the following relations

$$\mu_C = E_{M_6W_6C} - 6\mu_M - 6\mu_W \quad (5.11)$$

$$\mu_C = \frac{1}{2} \left[ E_{M_6W_6C_2} - 6\mu_M - 6\mu_W \right], \quad (5.12)$$

where  $E_{M_6W_6C}$  and  $E_{M_6W_6C_2}$  are the total energies per formula unit of the respective eta phase. By using Eq. (5.8) we may eliminate  $\mu_W$  and end up with

$$\mu_C = \frac{6E_{WC} - E_{M_6W_6C} - 6\mu_M}{5} \quad (5.13)$$

$$\mu_C = \frac{6E_{WC} - E_{M_6W_6C_2} - 6\mu_M}{4}. \quad (5.14)$$

In the DFT calculations we use the following formula to get the interface energy

$$\gamma = \frac{1}{A} \left[ E_{\text{system}} - \sum_{i \in \{W,C,M\}} \Delta N_i \mu_i - E_{\text{ref}} \right], \quad (5.15)$$

where  $E_{\text{system}}$  and  $E_{\text{ref}}$  is the total energy of the interface system and the corresponding bulk systems, respectively.  $\Delta N_i$  is the change in amount of component  $i$ , which is required for the non-stoichiometric interfaces.

For calculating adsorption and segregation energies, the expression

$$\Delta\gamma = \frac{1}{A} \left[ E_{\text{system}} + \sum_{i \in \{W,C,M\}} \Delta N_i \mu_i - E_{\text{system,ref}} \right] \quad (5.16)$$

is used, where  $E_{\text{system}}$  and  $E_{\text{system,ref}}$  are the total energies for the interface system with adsorbed/segregated binder phase atoms and for a reference interface system without adsorption/segregation, respectively.

## 5.2 Interface stress

Another important quantity, which is related to the interface free energy, is the interface stress  $\tau_{ij}$  [59]. The stress arises due to the different environment at the interface compared to the bulk. For example, at the surface of a metal the atomic

bonds are usually stronger than in the bulk since there are fewer bonds at the surface in which the valence electrons reside. As a consequence, the atoms at the surface would like to contract to get closer spacings. However, if the surface layer does not reconstruct and if no defects are introduced near the surface, the atomic spacing in the interface plane are equal to the ones in the bulk, i.e. it is completely coherent. Maintaining this coherency requires internal stresses parallel to the interface plane. The bulk thus exerts a tensile stress on the surface while the surface exerts a compressive stress on the bulk.

Since the stress exerted by the bulk and interface are parallel to the interface plane, the interface stress,  $\tau_{ij}$ , is a rank 2 tensor, and its dimension is the same as that for interface free energy and not to that of stress. The term *surface stress* is therefore a bit unfortunate. It is possible to obtain a relation between  $\tau_{ij}$  and  $\gamma$  if a small strain  $d\epsilon_{ij} = d\epsilon = \frac{dA}{A}$  is applied parallel to the interface. For simplicity we assume that the interface stress is independent on direction, i.e.  $\tau_{ij} = \tau$ . The change in  $G$  from the interface is  $d(\gamma A)$  and since the bulk is balancing the stress from the interface, the work done in stretching the bulk must be  $-\tau dA$ . Additionally, since the whole system is relaxed, i.e. there is no net stress on the system, the work involved in stretching, and thus the change in  $G$ , is zero. We therefore end up with

$$dG = d(\gamma A) - \tau dA = 0. \quad (5.17)$$

which may be simplified to

$$\tau = \gamma + A \frac{d\gamma}{dA}, \quad (5.18)$$

which is known as the Shuttleworth equation [86].

For a liquid surface, the last term of Eq. (5.18) is zero since the atoms are free to move to or away from the interface when it is strained [59]. The surface stress, which in this case is commonly called surface tension, is then equal to the surface free energy. In solids, however, the magnitude of  $A \frac{d\gamma}{dA}$  may be comparable to  $\gamma$ .

### 5.3 Wetting of surfaces

Wetting is an important technological parameter for many material processes including joining, solidification, and composite processing [81]. In the sintering of cemented carbides the wettability of the binder phase on the carbide is important to achieve desired densification. Wetting is a measure of the interfacial energies in a system, and is therefore a parameter associated with equilibrium thermodynamics. A concept related to wetting and of equal importance for technological processes is spreading, which is the rate by which a liquid spreads in contact area with a solid. However, this is a non-equilibrium process which can not be investigated using equilibrium interfacial energies. Wetting is fundamentally governed by the

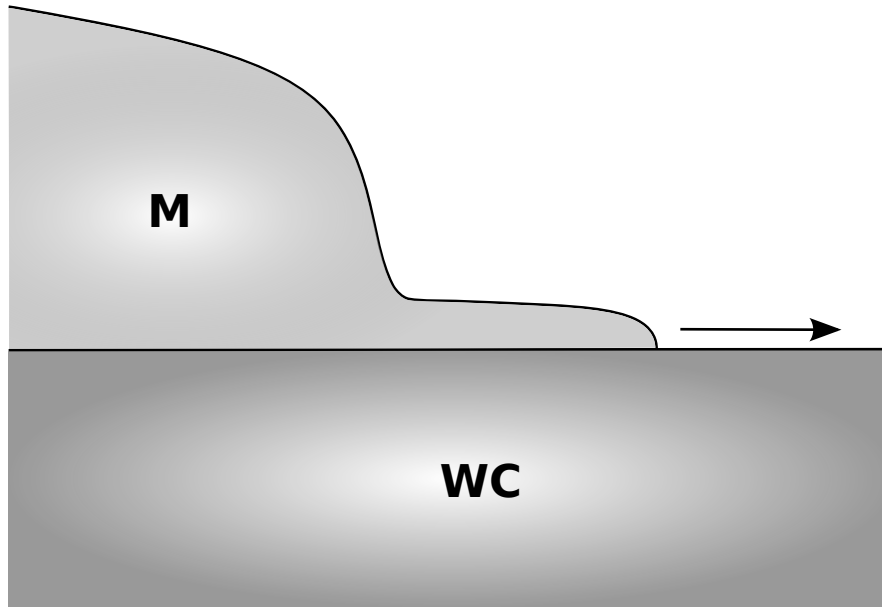


Figure 5.1: Figure showing spreading of binder phase (M) on a WC surface.

chemical content and atomic structure of the interfaces as well as bulk phases. In paper I, the wetting of WC surfaces by the binder phase in WC–Fe, WC–Co, and WC–Ni cemented carbides is investigated.

The degree by which the binder phase wets a WC surface is determined by the balance between the energies of the three different interfaces that are formed during the wetting; the WC surface energy  $\sigma_{WC}$ , the WC/M phase-boundary energy  $\gamma_{WC/M}$ , and the binder surface energy  $\sigma_M$ . A common measure of the degree of wetting is the spreading parameter  $S$ , which is defined as the difference in interface energy between the dry and wet case, i.e.

$$S = \sigma_{WC} - (\gamma_{WC/M} + \sigma_M). \quad (5.19)$$

This parameter gives the driving force for a spreading similar to the one shown in Fig. 5.1, where the WC surface area is replaced with equal areas of phase boundary and binder surface. However, it does not give any input on the kinetics of the spreading process. With the above definition of the spreading parameter, the binder phase is assumed to be taken from a reservoir, large enough in order to omit the change of reservoir surface area, which implies that the total surface area of the binder increases during the spreading process.

From Eq. (5.19) it follows that it is energetically favourable for the binder to spread on the carbide, i.e.  $S > 0$ , if the total interface energy is smaller in the wet case compared to the dry case. This situation is referred to as perfect wetting.

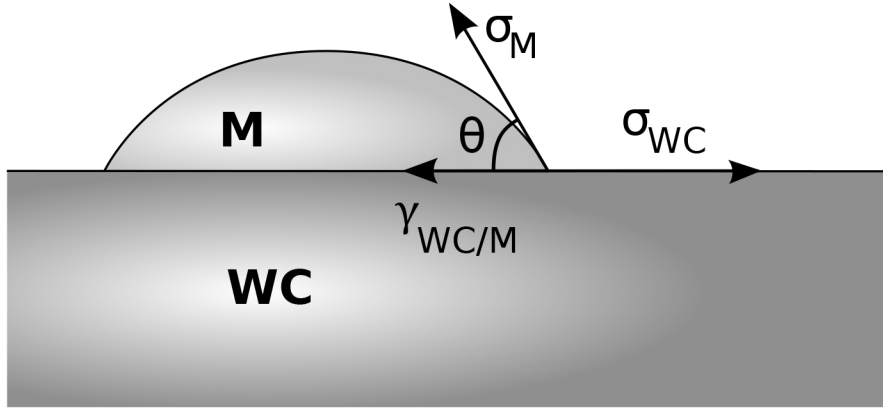


Figure 5.2: A binder (M) droplet on a WC surface with the contact angle  $\theta$ .

Otherwise, if spreading is unfavourable and  $S < 0$ , the wetting is only partial. The situation of partial wetting may be described by the contact angle  $\theta$  between the binder and the carbide that forms when a drop of binder is placed on a WC surface, see Fig. 5.2. Traditionally the angle is said to be determined by considering the force balance from the surface stresses (surface tensions) in the WC interface plane between the three interface energies, which yields the Young equation

$$\cos \theta = \frac{\sigma_{WC} - \gamma_{WC/M}}{\sigma_M}. \quad (5.20)$$

Combining the Young equation with the definition for  $S$  in Eq. (5.19) yields the Young-Dupré equation

$$\cos \theta = 1 + S/\sigma_{Co} \quad (S \leq 0). \quad (5.21)$$

If  $\theta = 180^\circ$ , the system is non-wetting, i.e. the droplet will not form any phase boundary with the substrate, and if  $\theta = 0^\circ$ , there is perfect wetting. The relations in Eqs (5.20) and (5.21) can be conveniently used for studying changes in wetting experimentally [87].

The approach of force balancing for relating  $\theta$  to the interface energies is not quite correct since there is no balance of forces perpendicular to the WC interface plane [87]. Further, as shown in Sec. 5.2, the interface stress is generally different from the interface free energy. There is another approach for relating  $\theta$  to the interface energy that will yield the same set of equations, but which only considers the interface energies: If the shape of the droplet is assumed to be a spherical cap, then the contact angle and volume (area in the 2D representation in Fig. 5.2) of the drop can be related. Further, knowing the shape and volume of the cap, allows for determination of interface areas. Then, minimizing the total interface energy

in the system under the constraint of preserving the volume of the drop then yields the relation in Eq. (5.20) [88]. This derivation only holds for droplets with the shape of a spherical cap, while in the presence of gravity the drop will deform. It is, however, possible to derive the Young equation, Eq. (5.20), for more general shapes of droplets that includes the presence of gravity [89, 90].

During sintering of WC-Co cemented carbides, a significant part of the densification occurs already during heating when the binder is still in the solid state [47]. This indicates that Co wets WC already before it melts while still in the solid state, and the same behaviour is expected for the other binders. When dealing with wetting with solid phases, the anisotropy of the interface energies and thus the crystal shapes should be taken into account [81]. Further, the concept of contact angle is not meaningful in a situation where a crystal wets a substrate since the apparent angle is highly sensitive to the anisotropic crystal shape. In paper I, we therefore focus on the driving force for wetting, i.e. the spreading parameter.

In 1965, Ramqvist [87] performed wetting experiments of pure liquid Fe, Co, and Ni on WC which indicated perfect wettability with  $\theta \approx 0$ . The pure formats of Fe, Co, and Ni are, however, not representative for the binder alloys in a cemented carbide. In a more recent study, Konyashin *et al.* investigated the wettability of liquid Co rich binder alloys on WC with a varying carbon content [91]. In the experiments four different binder alloys was used: one W-rich containing eta phase (alloy 1), one W-rich but without eta phase (alloy 2), one C-rich without graphite formation (alloy 3), and one C-rich with graphite formation (alloy 4). Cylinders of these four alloys was placed on top of WC substrates and subsequently heated under controlled conditions to melt the binder alloy. The alloys were then kept in the liquid state for 35 s before cooling. The resulting appearance of the alloys after melting and cooling can be seen in Fig. 5.3. It is apparent that the wettability decreases with increasing carbon content. The low carbon alloys show a perfect wetting of the WC substrate, but for the high carbon alloys the wetting is only partial. The wetting angles of alloy 3 and alloy 4 were measured to  $7^\circ$  and  $15^\circ$ , respectively, see Fig. 5.4. This increasing wettability with decreasing carbon content is in agreement with the increased shrinkage rate with decreasing carbon content during sintering observed by Bounhoure *et al.* in Refs [25, 26], see Sec. 2.1.5 .

### 5.3.1 Wetting of grain boundaries

The binder phase in cemented carbides can also wet WC/WC grain boundaries by infiltrating them and thus replacing the grain boundary for phase boundaries, see Fig. 5.5. To avoid confusion with the wetting of WC surfaces we refer to the wetting of WC/WC grain boundaries as WC/WC grain boundary infiltration. The driving force for infiltration can be assessed by calculating an infiltration parameter

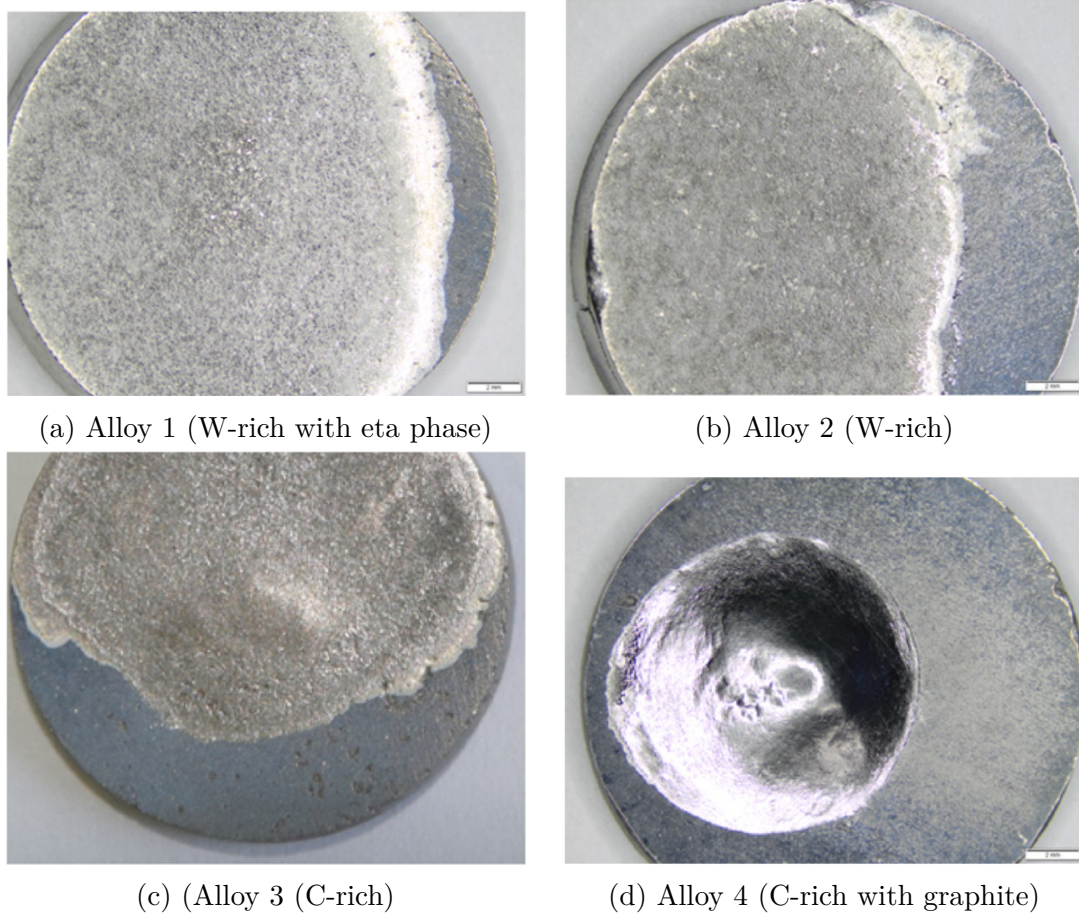
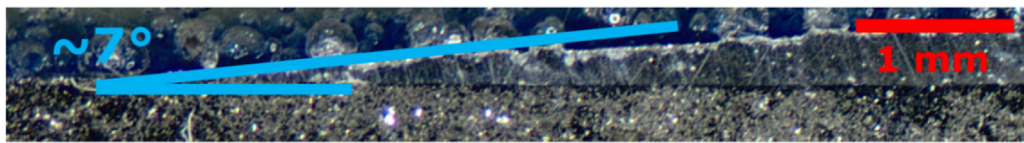


Figure 5.3: Appearance of binder alloys on WC substrates after melting and cooling, (a)-(d) [91].

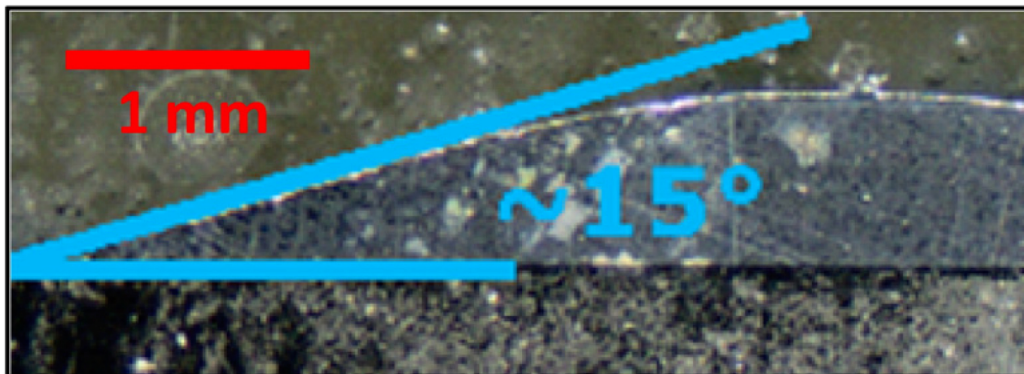
$W_{\text{inf}}$  equal to the difference in interface energy between the dry and wet case:

$$W_{\text{inf}} = \gamma_{\text{WC/WC}} - (\gamma_{\text{WC/M,1}} + \gamma_{\text{WC/M,2}}). \quad (5.22)$$

It is thus favorable to replace a WC/WC grain boundary with two WC/M phase boundaries, i.e there is a thermodynamic driving force for grain boundary infiltration, if  $W_{\text{inf}} > 0$ . Otherwise, if  $W_{\text{inf}} < 0$ , the grain boundary will resist being infiltrated by binder phase.



(a) Alloy 3 (C-rich)



(b) Alloy 4 (C-rich with graphite)

Figure 5.4: Cross sections and contact angles of alloy 3 and alloy 4 on WC substrate [91]

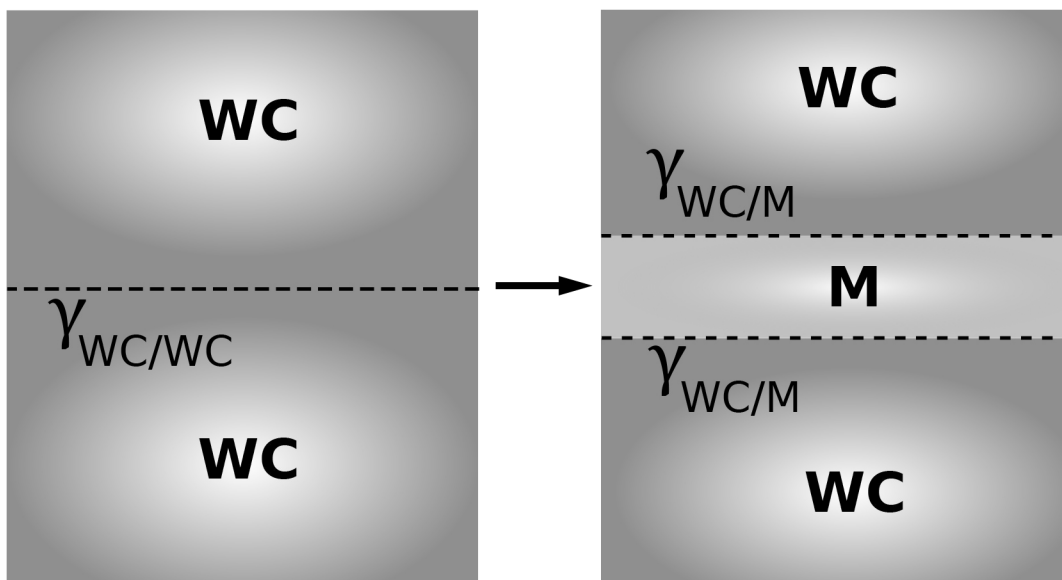


Figure 5.5: A schematic picture showing the energies involved in infiltrating a WC/WC grain boundary with binder phase (M).

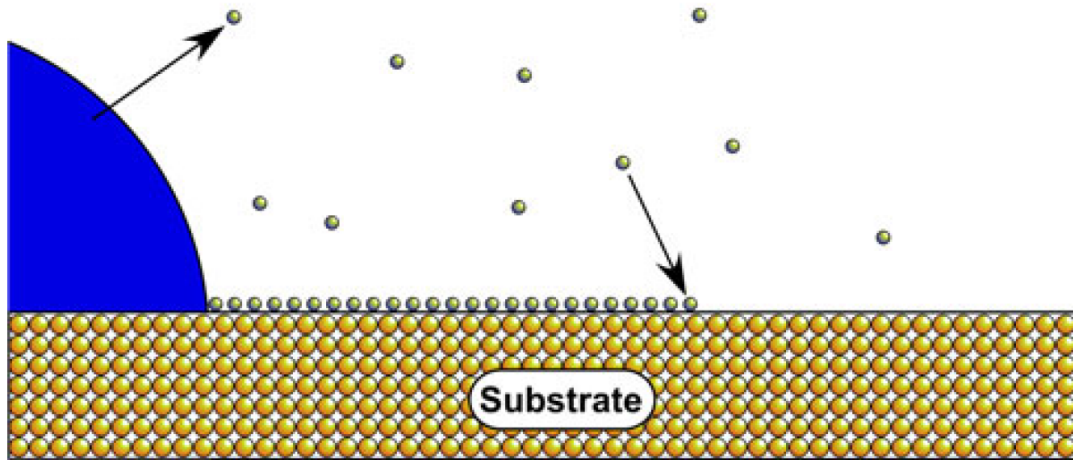


Figure 5.6: A schematic picture of the spreading of a liquid on a substrate, where the substrate surface can equilibrate by adsorbing atoms from the liquid phase either through the vapour phase or through diffusion along the substrate surface [81].

### 5.3.2 Effect from adsorption and segregation

Both the wetting of WC surfaces and WC/WC grain boundaries are sensitive to the local chemistry of the interfaces. Since the local chemistry effects the stoichiometry of the interfaces the dependence of the carbon content (carbon chemical potential) is also effected. If, for example, the stoichiometry of the equilibrated WC surface is different from that of the equilibrated WC/M phase boundary, the spreading parameter (Eq. (5.19)) will be sensitive to the carbon content in the material. This type of effect is investigated in paper I for WC surfaces and WC/WC grain boundaries.

Adsorption may also effect wetting and spreading differently as wetting is governed by the balance of equilibrated interface energies, while spreading is a kinetic process where equilibration of interfaces may or may not occur depending on the speed of the processes involved [81]. This is illustrated in Fig. 5.6, where a drop of liquid is spreading on a substrate where a precursor adsorbate of liquid phase atoms which either diffuse over the substrate or evaporate from the vapour and adsorb to the substrate surface. However, if the spreading is fast enough, the substrate will not equilibrate, and it is thus the clean substrate surface energy which is relevant for the driving force.

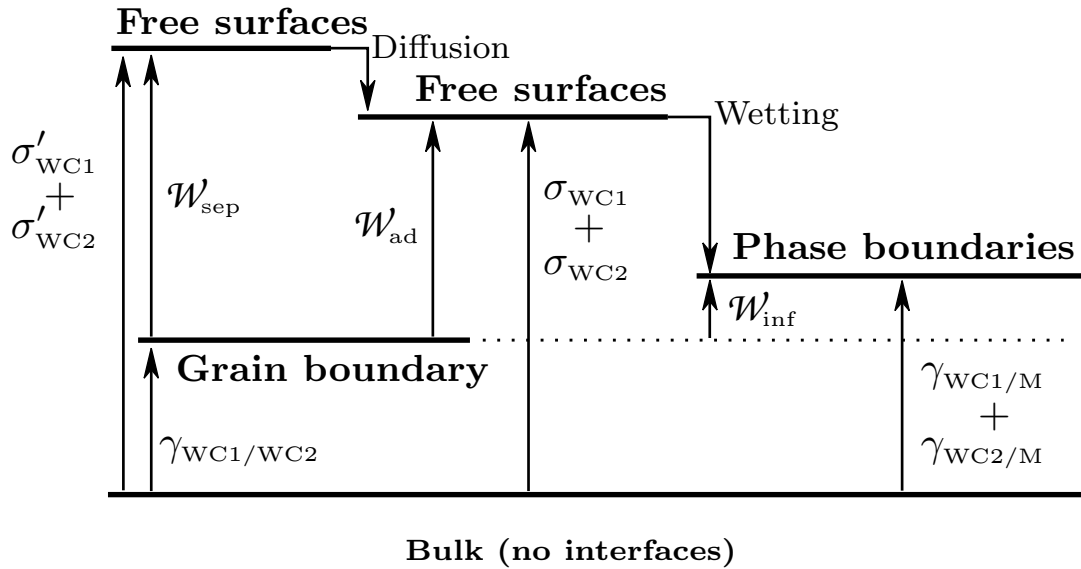


Figure 5.7: A diagram showing the energies involved in cleaving or infiltrating a WC/WC grain boundary, excluding plastic processes. This demonstrates the relation between  $\mathcal{W}_{sep}$ ,  $\mathcal{W}_{ad}$ , and  $\mathcal{W}_{inf}$ . This diagram has been adapted from an original diagram relating  $\mathcal{W}_{sep}$  and  $\mathcal{W}_{ad}$  presented in Ref. [94].

## 5.4 WC/WC grain boundary strength

The excellent mechanical properties of cemented carbides are highly dependent on the strength of its interfaces [52, 51, 92, 93]. In paper II, we investigate the segregation of binder phase atoms to WC/WC grain boundaries and its effect on the interface strength. The interface strength is measured in terms of the work of adhesion  $\mathcal{W}_{ad}$ , the work of separation  $\mathcal{W}_{sep}$ , and the work required to infiltrate the grain boundary with binder phase  $\mathcal{W}_{inf}$ . A diagram of how these quantities are related is seen in Fig. 5.7.

### 5.4.1 Work of adhesion

The work of adhesion  $\mathcal{W}_{ad}$  is the reversible free energy change associated with transforming an interface into two free surfaces while keeping the system in equilibrium with its environment [94]. Hence, this corresponds to slow decohesion. An explicit expression for the work of adhesion can be derived by consider a closed, isothermal system where two phases are in contact along an interface of area  $A_0$ . An external device work  $\mathcal{W}$  is required to separate the interface to two free surfaces under constant pressure  $P$  while keeping the chemical potentials  $\mu_i$  uniform among all parts

of the system, which in turn are allowed to exchange mass with one another. In order to quantify  $\mathcal{W}$  we return to Eqs. (5.1), (5.3), and (5.4), where  $E$  and  $G$  were defined. If multiple interfaces are included in the reversible change of the system, Eq. (5.1) becomes

$$dE = TdS - PdV + \sum_{i=1}^C \mu_i dN_i + \sum_{j=1}^D \gamma_j dA_j, \quad (5.23)$$

where  $D$  is the number of interfaces with interface free energy  $\gamma_j$  and area  $A_j$ . By using Eq. (5.4) the change in Gibbs energy  $dG$  becomes

$$dG = -SdT + VdP + \sum_{i=1}^C \mu_i dN_i + \sum_{j=1}^D \gamma_j dA_j. \quad (5.24)$$

From the definition of the process, all change in  $G$ , and hence the work done by the device, is covered by the interface term in Eq. (5.24), and we obtain

$$d\mathcal{W} = dG = \sum_{j=1}^D \gamma_j dA_j. \quad (5.25)$$

In the case of a WC/WC grain boundary this can be written as

$$d\mathcal{W} = \gamma_{\text{WC/WC}} dA_{\text{WC/WC}} + \sigma_{\text{WC1}} dA_{\text{WC1}} + \sigma_{\text{WC2}} dA_{\text{WC2}}, \quad (5.26)$$

where  $\sigma_{\text{WC1}, \text{WC2}}$  are the equilibrated surface energies,  $\gamma_{\text{WC/WC}}$  is the grain boundary energy and  $dA_i$  represents the change in their respective area. Here, the more common notation of  $\sigma$  for surface energies has replaced  $\gamma$ . From the definition of the process the surface areas should grow at the same rate  $dA = dA_{\text{WC1}} = dA_{\text{WC2}}$ , and this should in turn be the negative of the change in grain boundary area, i.e.  $dA = -dA_{\text{WC/WC}}$ . Consequently, Eq. (5.26) becomes

$$d\mathcal{W} = \left[ \sigma_{\text{WC1}} + \sigma_{\text{WC2}} - \gamma_{\text{WC/WC}} \right] dA. \quad (5.27)$$

The total work in the defined process is then

$$\mathcal{W} = \left[ \sigma_{\text{WC1}} + \sigma_{\text{WC2}} - \gamma_{\text{WC/WC}} \right] A_0. \quad (5.28)$$

The work of adhesion  $\mathcal{W}_{\text{ad}}$  should be expressed as work per area, and consequently

$$\mathcal{W}_{\text{ad}} = \sigma_{\text{WC1}} + \sigma_{\text{WC2}} - \gamma_{\text{WC/WC}}. \quad (5.29)$$

In an actual cleavage experiment, plastic processes require energy, and  $\mathcal{W}'_{\text{ad}}$  is, therefore, a lower limit to the actual work required in a cleavage experiment.

The work of adhesion for a general solid/liquid phase boundary may be written as

$$\mathcal{W}'_{\text{ad}} = \sigma_{\text{solid}} + \sigma_{\text{liquid}} - \gamma_{\text{solid/liquid}}. \quad (5.30)$$

If the liquid wets the solid partially, see Sec. 5.3,  $\mathcal{W}'_{\text{ad}}$  may be expressed in terms of the contact angle  $\theta$  and the liquid surface free energy  $\sigma_{\text{liquid}}$  according to

$$\mathcal{W}'_{\text{ad}} = \sigma_{\text{liquid}} (1 + \cos \theta). \quad (5.31)$$

This enables experimental measurements of the adhesion strength of solid/liquid interfaces.

### 5.4.2 Work of separation

The work of separation  $\mathcal{W}'_{\text{sep}}$  is the reversible work associated with cleaving the interface, neglecting plastic work and equilibration of the resulting surfaces through diffusion processes [94]. This, therefore, correspond to a fast decohesion. In the case of a WC/WC grain boundary it is defined as

$$\mathcal{W}'_{\text{sep}} = \sigma'_{\text{WC1}} + \sigma'_{\text{WC2}} - \gamma_{\text{WC/WC}}, \quad (5.32)$$

where  $\gamma_{\text{WC/WC}}$  and  $\sigma'_{\text{WC1,WC2}}$  is the grain boundary energy and the resulting unequilibrated surface energies, respectively. Since the equilibrated surface energies are lower than the unequilibrated ones, it follows that  $\mathcal{W}'_{\text{ad}} \leq \mathcal{W}'_{\text{sep}}$ . This is illustrated in Fig. 5.7.

In the DFT calculations in paper II,  $\mathcal{W}'_{\text{sep}}$  is obtained as the difference between the total energy of a grain boundary system  $E_{\text{system}}$  and a cleaved grain boundary system  $E_{\text{system,cleaved}}$ ,

$$\mathcal{W}'_{\text{sep}} = (E_{\text{system}} - E_{\text{system,cleaved}})/A, \quad (5.33)$$

where  $A$  is the interface area. However, there are many possible cleavage planes for each grain boundary, which correspond to different values of  $\mathcal{W}'_{\text{sep}}$ . The optimal cleavage plane is the one resulting in the lowest interface energy after separation, i.e. lowest  $\mathcal{W}'_{\text{sep}}$ . We therefore vary the cleavage plane and choose the one with lowest value of  $\mathcal{W}'_{\text{sep}}$ .

### 5.4.3 Work of infiltration by the binder phase

The work of infiltration  $\mathcal{W}'_{\text{inf}}$  is the work required to infiltrate a WC/WC grain boundary with binder phase and thereby replacing it with two phase boundaries,

see Fig. 5.5. It is therefore defined as

$$\mathcal{W}'_{\text{inf}} = \gamma_{\text{WC/M},1} + \gamma_{\text{WC/M},2} - \gamma_{\text{WC/WC}}, \quad (5.34)$$

where  $\gamma_{\text{WC/M},1}$  and  $\gamma_{\text{WC/M},2}$  are interface energies of the resulting phase boundaries. Since the phase boundary energies generally are much lower than the WC surface energies,  $\mathcal{W}'_{\text{inf}} \ll \mathcal{W}'_{\text{ad}}$ , which is illustrated in Fig. 5.7. The work of infiltration is the negative of the driving force for infiltration as defined in Sec. 5.3.1. With this definition of  $\mathcal{W}'_{\text{inf}}$ , infiltration is favourable if  $\mathcal{W}'_{\text{inf}} < 0$  and unfavourable if  $\mathcal{W}'_{\text{inf}} > 0$ . However, one can argue that in order to infiltrate the grain boundary it first has to be cleaved and then infiltrated (wetted) by binder phase. Consequently, even if infiltration is energetically favourable, the barrier for infiltration is still roughly given by  $\mathcal{W}'_{\text{sep}}$ . Alternatively, if the infiltration occurs through a diffusional process where atoms in the grain boundary are interchanged, the barrier is more related to the activation energy for diffusion.



## Conclusions and outlook

In the appended papers wetting and interfacial strength in WC–Fe, WC–Co, and WC–Ni cemented carbides are investigated using density functional theory. The local chemistry of interfaces is varied by substitution of W and C atoms for binder phase atoms.

The results from paper I indicate that the wettability of Ni on WC surfaces is potentially better compared to that of Co, while the wettability of Fe is worse than both others. Further, in all three cemented carbides the wetting is better in W-rich alloys compared to C-rich alloys, which is in agreement with experiments on shrinkage [25, 26] and wetting [91] in WC–Co.

In paper II we show that the segregation of binder phase atoms to WC/WC grain boundaries is in 0.5 monolayer proportion in essentially all studied grain boundaries in the three different cemented carbides. The segregation generally strengthens the grain boundaries regarding its resistance against fracture and infiltration by binder phase.

In both appended papers the DFT calculations are performed strictly at  $T = 0$  K, which is far from the relevant sintering and working temperatures for the materials. It would, therefore, serve as an important addition to the work in this thesis, to study the temperature dependence of interface energies. In such a study, DFT calculations are likely not feasible, especially not for the liquid state of the binder. Consequently, the use of methods such as analytical bond order potentials (ABOP), which are less expensive computationally, may become necessary.

Also, in the DFT calculations, we use both a model non-magnetic state and the ferromagnetic state of the binder phases to assess the effect from magnetic state on interface energies. However, at elevated temperatures, the binder phase is in the paramagnetic state where the local magnetic moments are disordered in contrast to the ferromagnetic state where they are ordered. The simulation of paramagnetic

state is obviously more complicated than ferromagnetic state. However, as the results from the paper I shows that binder surface and phase boundary energies are sensitive to the magnetic state, a study that included a more realistic magnetic description of the binder phase is of great interest.

## Computational method

The *computational method* chapter is intentionally left out of from the thesis. However, it will appear in the forthcoming PhD thesis where additional computational methods also will be presented. Here follows a brief description of the computational method used in the appended papers.

The calculations in the appended papers were performed with the density functional theory (DFT), which is a first-principles method, i.e. it does not require any experimental input but only atomic numbers and coordinates to make predictions. For more details on first-principles methods and DFT, the reader is referred to the book *Electronic Structure: Basic Theory and Practical Methods* by R.M. Martin [95]. The DFT calculations were performed with the plane-wave Vienna *ab-initio* simulation package (VASP) [96, 97]. The included projector-augmented wave (PAW) [98, 99] potentials and the Perdew, Burke, and Ernzerhof (PBE) exchange–correlation functional [100] were used. Further information about the settings and parameters used in VASP can be found in Ref. [34].



# Acknowledgments

First of all, I would like to thank my supervisor Göran Wahnström for being a supportive, knowledgeable, and patient supervisor, and for giving me the opportunity to pursue this work. I would also like to thank my co-workers Martin Petisme and Sven Johansson for discussions and guidance at the start of my project.

Everybody involved in the joint projects, including people from Sandvik, Seco Tools, KTH, Grenoble INP, and Materials Microstructure at Chalmers are acknowledged. The financial support from the Swedish Foundation for Strategic Research (SSF) and the Swedish Research Council (VR) is also acknowledged.

I would further like to thank all the members of the Materials and Surface Theory group and my co-advisor Hans-Olof André.

Lastly, I want to thank my fiancée Karolina and my son Sebastian for filling my life with love and joy.



# Bibliography

- [1] H E Exner. Physical and chemical nature of cemented carbides. *Int. Mater. Rev.*, 24:149–173, 1979.
- [2] Understanding cemented carbide. <http://www.destinytool.com/carbide-substrate.html>. Accessed: 2017-06-28.
- [3] B. Aronsson. *The origins and growth of cemented carbides*. Sandvik Group, Stockholm, 2005.
- [4] Leo Prakash. 1.02 - fundamentals and general applications of hardmetals. In Vinod K. Sarin, editor, *Comprehensive Hard Materials*, page 29. Elsevier, Oxford, 2014.
- [5] Turning re-invented - primeturning™ and coroturn® prime. <https://www.youtube.com/watch?v=nCYihCotzHw>. Accessed: 2017-07-04.
- [6] S. Norgren, J. Garcia, A. Blomqvist, and L. Yin. Trends in the p/m hard metal industry. *Int. J. Refract. Met. Hard Mater.*, 48:31, 2015.
- [7] Z. Zak Fang, Mark C. Koopman, and Hongtao Wang. 1.08 - cemented tungsten carbide hardmetal-an introduction. In Vinod K. Sarin, editor, *Comprehensive Hard Materials*, page 123. Elsevier, Oxford, 2014.
- [8] C.M. Fernandes and A.M.R. Senos. Cemented carbide phase diagrams: A review. *Int. J. Refract. Met. Hard Mater.*, 29:405, 2011.
- [9] T. W. Penrice. Alternative binders for hard metals. *J. Mater. Shaping Technol.*, 5:35–39, 1987.
- [10] V.A Tracey. Nickel in hardmetals. *Int. J. Refract. Met. Hard Mater.*, 11:137–149, 1992.
- [11] IJ Shon, KI Na, IY Ko, JM Doh, and JK Yoon. Effect of feal3 on properties of (w,t)c-feal3 hard materials consolidated by a pulsed current activated sintering method. *Ceram. Int.*, 38:5133–5138, 2012.

## Bibliography

---

- [12] JZ Long, ZJ Zhang, T. Xu, W. Peng, XY Wei, BZ Lu, and RQ Li. Wc-ni3al-b composites prepared through ni plus al elemental powder route. *Trans. Nonferrous Met. Soc. China*, 22:847–852, 2012.
- [13] M. Ahmadian, D. Wexler, T. Chandra, and A. Calka. Abrasive wear of wc-feal-b and wc-ni3al-b composites. *Int. J. Refract. Met. Hard Mater.*, 23:155 – 159, 2005.
- [14] Mehdi Ahmadian-Najafabadi, Materials University of Wollongong. School of Mechanical, and Mechatronic Engineering. Sintering, microstructure and properties of wc-feal-b and wc-ni3al-b composite materials, 2005.
- [15] B. Aronsson. Processing-properties relationship in cemented carbide. *Key Eng. Mater.*, 29-31:529, 1989.
- [16] J. W. Lee, D. Jaffrey, and J. D. Browne. Influence of process variables on sintering of WC-25 wt-%Co. *Powder Metall.*, 23(2):57, 1980.
- [17] G S Upadhyaya. *Cemented Tungsten Carbides: Production, Properties, and Testing*. Noyes Publications, 1 edition, 1998.
- [18] E Lassner and W-D Schubert. *Tungsten: Properties, Chemistry, Technology of the Element, Alloys, and Chemical Compounds*. Kluwer Academic/Plenum Publishers, 1999.
- [19] Pankaj K. Mehrotra. 1.07 - powder processing and green shaping. In Vinod K. Sarin, editor, *Comprehensive Hard Materials*, page 213. Elsevier, Oxford, 2014.
- [20] Thomas A. Wolfe, Thomas J. Jewett, and Raj P. Singh Gaur. 1.06 - powder synthesis. In Vinod K. Sarin, editor, *Comprehensive Hard Materials*, page 185. Elsevier, Oxford, 2014.
- [21] H.-O. Andrén. Microstructures of cemented carbides. *Mater. Des.*, 22:491, 2001.
- [22] Randall M. German. 1.08 - consolidation techniques. In Vinod K. Sarin, editor, *Comprehensive Hard Materials*, page 237. Elsevier, Oxford, 2014.
- [23] M. Göthelid, S. Haglund, and J. Ågren. Influence of O and Co on the early stages of sintering of WC-Co: A surface study by AES and STM. *Acta Mater.*, 48:4357, 2000.
- [24] J. Kishino, H. Nomura, S.-G. Shin, H. Matsubara, and T. Tanase. Computational study on grain growth in cemented carbides. *Int. J. Refract. Met. Hard Mater.*, 20:31, 2002.

- 
- [25] V. Bounhoure, J. M. Missiaen, S. Lay, and E. Pauty. Discussion of nonconventional effects in solid-state sintering of cemented carbides. *J. Am. Ceram. Soc.*, 92:1396, 2009.
- [26] V. Bounhoure, S. Lay, F. Charlot, A. Antoni-Zdziobek, E. Pauty, and J.M. Missiaen. Effect of c content on the microstructure evolution during early solid state sintering of wc-co alloys. *Int. J. Refract. Met. Hard Mater.*, 44:27, 2014.
- [27] A. Fernández Guillermet. Thermodynamic properties of the co-w-c system. *Metall. Trans. A*, 20A:935, 1989.
- [28] A. Fernández Guillermet. The co-fe-ni-w-c phase diagram: a thermodynamic description and calculated sections for (co-fe-ni) bonded cemented wc tools. *Z. Metallkd.*, 80:83, 1989.
- [29] Gopal S. Upadhyaya. 2 - crystal structure and phase equilibria. In Gopal S. Upadhyaya, editor, *Cemented Tungsten Carbides*, pages 7 – 54. William Andrew Publishing, Westwood, NJ, 1998.
- [30] Sabine Lay and Jean-Michel Missiaen. 1.03 - microstructure and morphology of hardmetals. In Vinod K. Sarin, editor, *Comprehensive Hard Materials*, page 91. Elsevier, Oxford, 2014.
- [31] A. S. Kurlov and A. I. Gusev. Tungsten carbides and w-c phase diagram. *Inorg. Mater.*, 42(2):121, 2006.
- [32] A. A. Rempel, R. Würschum, and H.-E. Schaefer. Atomic defects in hexagonal tungsten carbide studied by positron annihilation. *Phys. Rev. B*, 61:5945, 2000.
- [33] J Weidow, S A E Johansson, H-O Andrén, and G Wahnström. Transition metal solubilities in WC in cemented carbide materials. *J. Am. Ceram. Soc.*, 94:605–610, 2011.
- [34] M V G Petisme, S A E Johansson, and G Wahnström. A computational study of interfaces in WC-Co cemented carbides. *Model. Simul. Mater. Sc.*, 23:045001, 2015.
- [35] Mikael Christensen, Göran Wahnström, C Allibert, and S Lay. Quantitative analysis of wc grain shape in sintered wc-co cemented carbides. *Phys. Rev. Lett.*, 94:066105, 2005.
- [36] S. Lay, D. Donnadiou, and M. Loubradou. Polarity of prismatic facets delimiting WC grains in WC-Co alloys. *Micron*, 41:472, 2010.

## Bibliography

---

- [37] Bernhard Wittmann, Wolf-Dieter Schubert, and Benno Lux. {WC} grain growth and grain growth inhibition in nickel and iron binder hardmetals. *Int. J. Refract. Met. Hard Mater.*, 20:51, 2002.
- [38] M. B. Stearns. 1.1.2.2 phase diagrams, lattice constants and elastic moduli: Datasheet from landolt-börnstein - group iii condensed matter · volume 19a: “3d, 4d and 5d elements, alloys and compounds” in springermaterials, 1986.
- [39] T. Nishizawa and K. Ishida. The co (cobalt) system. *Bulletin of Alloy Phase Diagrams*, 4:387–390, 1983.
- [40] Jonathan Weidow and Hans-Olof Andréén. Binder phase grain size in wc-co-based cemented carbides. *Scr. Mater.*, 63:1165, 2010.
- [41] K.P. Mingard, B. Roebuck, J. Marshall, and G. Sweetman. Some aspects of the structure of cobalt and nickel binder phases in hardmetals. *Acta Mater.*, 59:2277, 2011.
- [42] K. Hilpert, D. Kobertz, V. Venugopal, M. Miller, H. Gerads, F. J. Bremer, and H. Nickel. Phase diagram studies on the al-ni system. *Z. Naturforsch. pt. A*, 42:1327–1332, 1987.
- [43] Max Hansen and Kurt Anderko. *Constitution of binary alloys*. McGraw-Hill, New York, 2. edition, 1958.
- [44] W. M. Haynes, editor. *CRC Handbook of Chemistry and Physics*. CRC Press/Taylor and Francis, Boca Raton, FL, 97th edition, 2016. Internet version accessed January 2017.
- [45] B. Legendre and M. Sghaier. Curie temperature of nickel. *J. Therm. Anal. Calorim.*, 105:141–143, 2011.
- [46] John Chipman. Thermodynamics and phase diagram of the fe-c system. *Metall. Trans*, 3:55–64, 1972.
- [47] C. H. Allibert. Sintering features of cemented carbides WC-Co processed from fine powders. *Int. J. Refract. Met. Hard Mater.*, 19:53, 2001.
- [48] C.-S. Kim, T. R. Massa, and G. S. Rohrer. Interface character distributions in WC-Co composites. *J. Am. Ceram. Soc.*, 91:996, 2008.
- [49] Chang-Soo Kim and Gregory S. Rohrer. Geometric and crystallographic characterization of wc surfaces and grain boundaries in wc-co composites. *Interface Sci.*, 12:19, 2004.

- 
- [50] S. Hagège, J. Vicens, G. Nouet, and P. Delavignette. Analysis of structure defects in tungsten carbide. *Phys. Status Solidi A*, 61:675, 1980.
- [51] G. Östberg, K. Buss, M. Christensen, S. Norgren, H.-O. Andrén, D. Mari, G. Wahnström, and I. Reineck. Effect of TaC on plastic deformation of WC-Co and Ti(C,N)-WC-Co. *Int. J. Refract. Met. Hard Mater.*, 24:145, 2006.
- [52] D. Mari, S. Bolognini, G. Feusier, T. Viatte, and W. Benoit. Experimental strategy to study the mechanical behaviour of hardmetals for cutting tools. *Int. J. Refract. Met. Hard Mater.*, 17:209, 1999.
- [53] D. Mari, U. Marti, and P. C. Silva. A new photolithographic technique to detect the local deformation of materials: application to wc co composites. *Mater. Sci. Eng. A*, 158:203, 1992.
- [54] Karin Mannesson, Mattias Elfving, Alexandra Kusoffsky, Susanne Norgren, and John Ågren. Analysis of wc grain growth during sintering using electron backscatter diffraction and image analysis. *Int. J. Refract. Met. Hard Mater.*, 26:449, 2008.
- [55] A. Henjered, M. Hellsing, H. O. Andrén, and H. Nordén. Quantitative microanalysis of carbide/carbide interfaces in wc-co-base cemented carbides. *Mater. Sci. Technol.*, 2:847, 1986.
- [56] J. Weidow and H.-O. Andrén. Apt analysis of WC-Co based cemented carbides. *Ultramicroscopy*, 111:595, 2011.
- [57] Jonathan Weidow and Hans-Olof Andrén. Grain and phase boundary segregation in wc-co with small v, cr or mn additions. *Acta Mater.*, 58:3888, 2010.
- [58] Jonathan Weidow and Hans-Olof Andrén. Grain and phase boundary segregation in wc-co with small v, cr or mn additions. *Acta Mater.*, 58:3888, 2010.
- [59] A.P. Sutton and R.W. Balluffi. *Interfaces in crystalline materials*. Monographs on the physics and chemistry of materials. Clarendon Press, 1995.
- [60] V. Randle. Role of grain boundary plane in grain boundary engineering. *Mater. Sci. Technol.*, 26:774, 2010.
- [61] R. C. Pond and W. Bollmann. The symmetry and interfacial structure of bicrystals. *Philos. Trans. R. Soc. London, Ser. A*, 292(1395):449, 1979.

## Bibliography

---

- [62] S. Hagège, G. Nouet, and P. Delavignette. Grain boundary analysis in tem. iv. coincidence and the associated defect structure in tungsten carbide. *physica status solidi (a)*, 62:97, 1980.
- [63] J. Vicens, M. Benjdir, G. Nouet, A. Dubon, and J. Y. Laval. Cobalt intergranular segregation in wc-co composites. *J. Mater. Sci.*, 29:987, 1994.
- [64] S. Lay and M. Loubradou. Characteristics and origin of clusters in submicron wc-co cermets. *Philos. Mag.*, 83:2669, 2003.
- [65] Vineet Kumar, Zhigang Zak Fang, S. I. Wright, and M. M. Nowell. An analysis of grain boundaries and grain growth in cemented tungsten carbide using orientation imaging microscopy. *Metallurgical and Materials Transactions A*, 37:599, 2006.
- [66] Jong-Dae Kim, Suk-Joong L. Kang, and Joo-Wan Lee. Formation of grain boundaries in liquid-phase-sintered wc-co alloys. *J. Am. Ceram. Soc.*, 88:500, 2005.
- [67] Sabine Lay and Jean-Michel Missiaen. Atomic structure of the  $\Sigma = 2$  twist carbide grain boundary in wc-co alloys. *Phil. Mag.*, 93:1146, 2013.
- [68] A.E. Johansson, Sven, Martin Petisme, and Göran Wahnström. A computational study of special grain boundaries in wc-co cemented carbides. *Comput. Mater. Sci.*, 98:345, 2015.
- [69] Mikael Christensen and Göran Wahnström. Effects of cobalt intergranular segregation on interface energetics in wc-co. *Acta Mater.*, 52:2199, 2004.
- [70] Mikael Christensen and Göran Wahnström. Co-phase penetration of wc ( $10\bar{1}0$ ) / wc ( $10\bar{1}0$ ) grain boundaries from first principles. *Phys. Rev. B*, 97:115415, 2003.
- [71] Y. Wang, M. Heusch, S. Lay, and C.H. Allibert. Microstructure evolution in the cemented carbides wc-co i. effect of the c/w ratio on the morphology and defects of the wc grains. *Phys. Status Solidi A*, 193:271, 2002.
- [72] V. Bounhoure, S. Lay, M. Loubradou, and J. M. Missiaen. Special wc/co orientation relationships at basal facets of wc grains in wc-co alloys. *J. Mater. Sci.*, 43:892, 2008.
- [73] S. Lay, S. Hamar-Thibault, and A. Lackner. Location of vc in vc, cr<sub>3</sub>c<sub>2</sub> codoped wc-co cermets by hrem and eels. *Int. J. Refract. Met. Hard Mater.*, 20:61, 2002.

- 
- [74] S. Lay, S. Hamar-Thibault, and M. Loubradou. Accommodation of the lattice mismatch at the vcx-wc interface. *Interface Sci.*, 12:187, 2004.
- [75] S A E Johansson and G Wahnström. Theory of ultrathin films at metal–ceramic interfaces. *Philos. Mag. Lett.*, 90:599, 2010.
- [76] S A E Johansson and G Wahnström. A computational study of thin cubic carbide films in WC/Co interfaces. *Acta Mater.*, 59:171, 2011.
- [77] K. Mohan and P.R. Strutt. Observation of co nanoparticle dispersions in wc nanograins in wc-co cermets consolidated from chemically synthesized powders. *Nanostruct. Mater.*, 7:547, 1996.
- [78] K. Mohan and P.R. Strutt. Microstructure of spray converted nanostructured tungsten carbide-cobalt composite. *Mater. Sci. Eng., A*, 209:237, 1996.
- [79] Tetsuya Suzuki, Kunio Shibuki, Toshiyuki Suzuki, and Yuichi Ikuhara. Grain boundary in cemented carbide. *Philos. Mag. Lett.*, 71:289, 1995.
- [80] Maxime Pellan. *Development of grain boundaries and phase boundaries in WCCo cemented carbides*. PhD thesis, Université Grenoble Alpes, 2015.
- [81] Wayne D. Kaplan, Dominique Chatain, Paul Wynblatt, and W. Craig Carter. A review of wetting versus adsorption, complexions, and related phenomena: the rosetta stone of wetting. *J. Mater. Sci.*, 48:5681, 2013.
- [82] Guo-Xin Qian, Richard M. Martin, and D. J. Chadi. First-principles study of the atomic reconstructions and energies of ga- and as-stabilized gaas(100) surfaces. *Phys. Rev. B*, 38:7649, 1988.
- [83] Karsten Reuter and Matthias Scheffler. Composition, structure and stability of ruo<sub>2</sub>(110) as a function of oxygen pressure. *Phys. Rev. B*, 65:035406, 2001.
- [84] P. Gustafson. An evaluation of the thermodynamic properties and the *P, T* phase diagram of carbon. *Carbon*, 24(2):169, 1986.
- [85] J. M. Newsam, A. J. Jacobson, L. E. McCandlish, and R. S. Polizzotti. The structures of the  $\eta$ -carbides Ni<sub>6</sub>Mo<sub>6</sub>C, Co<sub>6</sub>Mo<sub>6</sub>C, and Co<sub>6</sub>Mo<sub>6</sub>C<sub>2</sub>. *J. Solid State Chem.*, 75:296, 1988.
- [86] R. Shuttleworth. The surface tension of solids. *Proc. Phys. Soc. London, Sect. A*, 63:444, 1950.
- [87] L Ramqvist. Wetting of metallic carbides by liquid copper, nickel, cobalt, and iron. *Int. J. Powder Metall.*, 1:2, 1965.

## Bibliography

---

- [88] Gene Whyman, Edward Bormashenko, and Tamir Stein. The rigorous derivation of young, cassie–baxter and wenzel equations and the analysis of the contact angle hysteresis phenomenon. *Chem. Phys. Lett.*, 450:355, 2008.
- [89] P. Roura and Joaquim Fort. Local thermodynamic derivation of young’s equation. *J. Colloid Interface Sci.*, 272:420, 2004.
- [90] Lasse Makkonen. Young’s equation revisited. *J. Phys. Condens. Matter*, 28:135001, 2016.
- [91] I. Konyashin, A.A. Zaitsev, D. Sidorenko, E.A. Levashov, B. Ries, S.N. Konishev, M. Sorokin, A.A. Mazilkin, M. Herrmann, and A. Kaiser. Wettability of tungsten carbide by liquid binders in wc–co cemented carbides: Is it complete for all carbon contents? *Int. J. Refract. Met. Hard Mater.*, 62, Part B:134, 2017.
- [92] M. V. G. Petisme, S. Johansson, and G. Wahnström. Molecular dynamics simulations of wc/wc grain boundary sliding: the effect of thin cobalt films on sliding resistance. *Proceedings of the 18th Plansee Seminar*, 2013.
- [93] M. V. G. Petisme, M. A. Gren, and G. Wahnström. Molecular dynamics simulation of WC/WC grain boundary sliding resistance in WC-Co cemented carbides at high temperature. *Int. J. Refract. Met. Hard Mater.*, 49:75, 2015.
- [94] M W Finnis. The theory of metal-ceramic interfaces. *J. Phys.: Condens. Matter*, 8:5811, 1996.
- [95] R.M. Martin. *Electronic Structure: Basic Theory and Practical Methods*. Cambridge University Press, 2004.
- [96] G. Kresse and J. Furthmüller. Efficient iterative schemes for ab initio total-energy calculations using a plane-wave basis set. *Phys. Rev. B*, 54:11169, 1996.
- [97] G. Kresse and J. Furthmüller. Efficiency of ab-initio total energy calculations for metals and semiconductors using a plane-wave basis set. *Comp. Mater. Sci.*, 6:15, 1996.
- [98] P. E. Blöchl. Projector augmented-wave method. *Phys. Rev. B*, 50:17953, 1994.
- [99] G. Kresse and D. Joubert. From ultrasoft pseudopotentials to the projector augmented-wave method. *Phys. Rev. B*, 59:1758, 1999.

- [100] J. P. Perdew, K. Burke, and M. Ernzerhof. Generalized gradient approximation made simple. *Phys. Rev. Lett.*, 77:3865, 1996.

